Simultaneous Spectroscopic Determination of Ion Temperature, Electron Density, and Magnetic Field for the ZaP-HD Experiment

Lorcan Padraig Joseph McGonigle

A thesis
submitted in partial fulfillment of the
requirements for the degree of

Master of Science in Aeronautics & Astronautics

University of Washington

2015

Committee:

Uri Shumlak, Chair

Brian A. Nelson

Program Authorized to Offer Degree:
Aeronautics and Astronautics

University of Washington

Abstract

Simultaneous Spectroscopic Determination of
Ion Temperature, Electron Density, and Magnetic Field
for the ZaP-HD Experiment

Lorcan Padraig Joseph McGonigle

Chair of the Supervisory Committee:
Professor Uri Shumlak
Aeronautics and Astronautics

For over a decade, the ZaP Flow Z-Pinch experiment has demonstrated a sheared-flow stabilized Z-pinch, a linear plasma configuration with longitudinal current flow and azimuthal magnetic field confinement. A recent upgrade to the ZaP experiment, named ZaP-HD, looks to investigate the scaling relation that could plot its course towards a viable fusion reactor. This thesis documents the simultaneous measurement of the key magnetohydrodynamic parameters of ion temperature, electron density, and magnetic field on the ZaP-HD experiment. Temperature, electron density, and magnetic field each contribute a unique line-altering mechanism to the line radiation emitted from the ZaP-HD plasma. Through a least-squares fit in both the natural and Fourier domain to the emission spectrum of a C IV line at 581.2 nm known a priori to have the form of a Voigt profile, each of the desired parameters can be resolved for sufficiently small noise levels. Noise levels, defined as the ratio of the standard deviation of the noise in a dark region of the spectrum to the peak signal amplitude, at or below around 1% provide measurements corroborated by other diagnostics on the ZaP-HD experiment.

ACKNOWLEDGMENTS

I would like to begin by thanking Professor Uri Shumlak for opening the doors to the ZaP-HD experiment, teaching three incredible courses, and answering too many questions to count. I couldn't have been luckier to have had such a presence in my graduate education. I am likewise indebted to Dr. Raymond Golingo for sharing his wealth of experience, knowledge, and enthusiasm, each of which played an integral role in the completion of this thesis. I would also like to thank Professor Brian Nelson for his timely and astute comments. Lastly, I would like to thank Mike Hughes, Mike Ross, and the rest of the ZaP team for their guidance and support. I look forward to the day that flow Z-pinches power the world!

si vitiis mediocribus ac mea paucis mendosa est natura... causa fuit parentes

Contents

Chapter 1

Introduction

Controlled nuclear fusion offers economically and ecologically sustainable energy at an energy scale commensurate to the vociferous and ever increasing demands of a modern power grid. To achieve nuclear fusion, the nuclei of two appropriate atoms must be brought close enough together for the Coulombic repulsion of like-charged electrons to be superseded by the strong nuclear force. Thus, the challenge of nuclear fusion is to create highly energetic particles sufficiently directed so as to interact before dissipative mechanisms intercede. In stellar environments, large mass densities provide sufficient gravitation to maintain plasma configurations for sustained fusion. On more human scales, fusion is approached through some combination of inertial and magnetic confinement. Magnetic confinement, in particular, has shown promise as a means of confining and insulating a hot plasma long enough for fusion to take place.

However, the three orders of magnitude that separate the mass of an electron from the mass of an ion coupled to the inherently kinetic processes of a gas produce dynamics that cover many orders of spatial and temporal scales. This breadth of scale offers many opportunities for instabilities to destroy confinement. The ZaP experiment investigates the stabilizing effect of a sheared velocity profile embedded in a Z-pinch, a linear plasma configuration with longitudinal current and azimuthal magnetic field.

Because of its simplicity and hereto demonstrated stability [1], the ZaP experiment is uniquely

positioned as an economically sound fusion concept. More recent work on the ZaP experiment posits that it should scale agreeably to achieve a high energy density plasma (HEDP) [7] making it a preeminent fusion reactor concept. Should all else fail, because of the plasma's linear configuration and diagnostic access that a Z-pinch provides, the ZaP experiment remains an opportunity for fundamental plasma science with applications to astrophysical phenomena and other fusion reactor concepts.

1.1 The ZaP Flow Z-Pinch experiment

The ZaP experiment improves upon the static Z-pinch by embedding a sheared velocity profile into the bulk plasma flow, such that the plasma at the edge of the pinch moves with a different speed than the plasma at the core of the pinch. Previous analytical and computational work have demonstrated that supplying sufficient shear precludes the two dominant, large-scale instabilities that plague static Z-pinches. These two instabilities, referred to as the sausage and kink modes for their characteristic shape can be derived from ideal magnetohydrodynamics (MHD), a single-fluid plasma model for large spatial scale and low temporal frequency phenomenon. As the simplest physical model for plasma dynamics, MHD is the beginning for any stability analysis of a magnetic confinement topology. A further discussion of these MHD modes is provided in a section 2.1. A cross section of the ZaP-HD experiment can be seen below in Figure 1.1.

1.1.1 Diagnostics on ZaP-HD

The investigation of the broad range of plasma phenomena necessitates a broad range of diagnostics. Plasmas are fast, hot, and complex. Thus, observing plasmas offers an exciting set of challenges that mix the need for high temporal and spatial resolution with the requirement that the diagnostic should not alter the plasma's state–a constraint not typically seen at macroscopic scales.

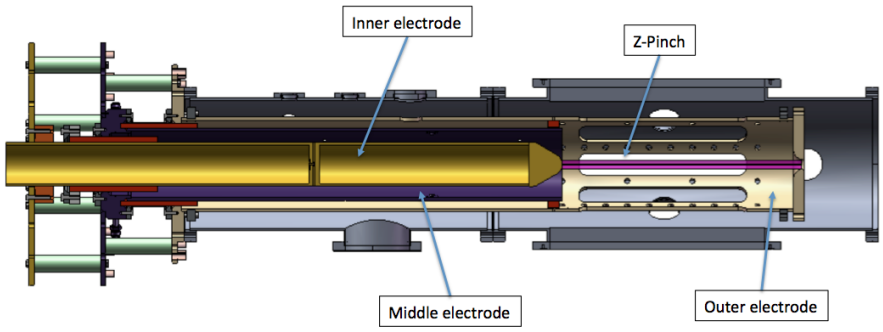

Figure 1.1 A cross section of the ZaP-HD machine, as shown in [8], shows the inner, middle, and outer electrodes, as well as the location of the Z-pinch.

To better understand plasma behavior the ZaP-HD experiment is equipped with several diagnostics. This thesis focuses on the spectroscopy system. Through the observation of the intensity of light as a function of wavelength emitted from the plasma, the plasma's ion temperature, electron density, and magnetic field can be radially resolved; going forward, the ion temperature will not be differentiated from the electron temperature, as Thomson scattering observations demonstrated that on ZaP the two are roughly equivalent [3]. While the rest of this thesis focuses on spectroscopy, we briefly introduce some of the other diagnostics found on the ZaP-HD experiment. These non-spectroscopic diagnostics will be used later in this thesis as corroborating instruments.

There are two main classes of diagnostics presently used on ZaP-HD. The first class measures the magnetic field through Faraday's Law, whereby a changing magnetic flux induces a voltage across a loop. The voltage can then be digitized and numerically integrated, passively integrated with an RC circuit, or actively integrated with an operational amplifier to determine the magnetic flux. On the ZaP-HD experiment, the latter is performed by the magnetic probes that sit in azimuthal arrays on the inner edge of the vacuum vessel wall. These magnetic probes were used to check the magnetic field values measured from the Zeeman splitting of a C IV line.

The second class of diagnostics measures plasma parameters through the optical properties of a plasma. The ZaP-HD experiment has a 4-chord heterodyne interferometer and a digital hologra-

phy set up. The interferometer is capable of measuring the line-integrated electron density along the lines of intersection between the plasma and laser beams. The digital holographic interferometer (DHI) system, through a similar process, records the two-dimensional line-integrated electron density where the laser beam intersects the plasma. Together, the magnetic probes and interferometer/DHI provide bounds on the spectroscopic measurement of electron density and magnetic field strength. However, in this thesis only the interferometer was used to check electron density measurements.

1.1.2 Spectroscopy

Through the observation of the intensity of light as a function of wavelength emitted from the plasma, spectroscopy offers a non-perturbative diagnostic with the potential to radially resolve the plasma's temperature, electron density, velocity, and magnetic field. Of course there is a wide variety of light emitted from a plasma, e.g. bremsstrahlung, black body, line, etc. ZaP's spectroscopy system observes line radiation, i.e., the light emitted during the deexcitation of an electron still bound within an ion. This transition is sensitive to the properties of the radiator, the particles around it, and any background fields. Thus, through the observation of the distribution of known transitions the environment of the radiator can be ascertained. Additional a priori assumptions of plasma geometry allow such observations to produce radially resolved plasma parameters.

To better explicate this process the next section provides a brief overview of the relevant plasma and spectroscopic theory. Following this Theory section, an overview of the spectroscopy set up is provided in the Experimental Design section. Subsequently, the fourth section, Data Analysis, describes the Fourier transform least-squares fit used to determine the desired plasma parameters; this includes a discussion of the maximum noise level for successful deconvolution and the presentation of some exemplar data. The final section provides some concluding remarks on the state of this spectroscopy system and opportunities for future work.

Chapter 2

Relevant Background Theory

We now turn to a brief overview of the theory that describes the plasma dynamics of a Z-pinch equilibrium and its stability. Following this brief introduction to magnetohydrodynamics (MHD), we then focus on line radiation and the line-altering mechanisms (Doppler, Stark, and Zeeman effects) of interest for our experiment.

2.1 Magnetohydrodynamics and the sheared flow Z-pinch

The ZaP experiment improves upon the static Z-pinch by embedding a sheared velocity profile into the bulk plasma flow, such that the plasma at the edge of the pinch moves with a different speed than the plasma at the core of the pinch. Previous analytical and computational work have demonstrated that supplying sufficient shear precludes the two dominant, large-scale instabilities that plague static Z-pinches. These two instabilities, referred to as the sausage and kink modes for their characteristic shape, can be derived from ideal magnetohydrodynamics (MHD), a single-fluid plasma model for large spatial scale and low temporal frequency phenomena.

As the simplest physical model for plasma dynamics, MHD is the beginning for any stability

analysis of a magnetic confinement topology. MHD is governed by the coupled set of equations:

$$\frac{\partial \rho}{\partial t} + \nabla \cdot \rho \vec{v} = 0 \tag{2.1a}$$

$$\rho \frac{d\vec{v}}{dt} = \vec{J} \times \vec{B} - \nabla p \tag{2.1b}$$

$$\frac{d}{dt}(p/\rho^{\gamma}) = 0 \tag{2.1c}$$

$$\vec{E} + \vec{v} \times \vec{B} = 0 \tag{2.1d}$$

$$\nabla \times \vec{E} = -\frac{\partial \vec{B}}{\partial t} \tag{2.1e}$$

$$\nabla \times \vec{B} = \mu_o \vec{J} \tag{2.1f}$$

$$\nabla \cdot \vec{B} = 0, \tag{2.1g}$$

where ρ is the mass density of the plasma, $\vec{v}$ is the velocity, $\vec{J}$ is the current density, $\vec{B}$ is the magnetic field, p is the plasma pressure, γ is the ratio of specific heats, $\vec{E}$ is the electric field, and μ_o is the permeability of free space. The reader is referred to [4] for a derivation of the MHD equations from Maxwell's equations coupled to a Boltzmann equation for each species present.

The equilibrium of a Z-pinch is described by the radial component of the force balance equation, (2.1b), coupled with Ampère's Law, (2.1f),

$$\frac{B_\theta}{\mu_o r}\frac{\partial (rB_\theta)}{\partial r} + \frac{\partial p}{\partial r} = 0. \tag{2.2}$$

The stability of a Z-pinch can then be analyzed using linear stability analysis. First the perturbation, ξ_i, is expanded in azimuthal Fourier modes, such that $\vec{\xi} = \vec{\xi}(r,z,t)e^{im\phi}$. Then a variational method is employed to determine the minimum energy state of the Z-pinch equilibrium under such perturbations, i.e. $\int \vec{F}[\vec{\xi}] \cdot \vec{\xi}$, where $\vec{F}$ is the MHD force operator defined as

$$\vec{F[\xi]} = \nabla(\vec{\xi} \cdot \nabla p_o + \Gamma p_o \nabla \cdot \vec{\xi}) + \frac{1}{\mu_o}([\nabla \times \vec{B_o}] \times [\nabla \times (\vec{\xi} \times \vec{B_o})] + [\nabla \times \nabla \times (\vec{\xi} \times \vec{B_o})] \times \vec{B_o}). \tag{2.3}$$

This yields the following requirement on plasma pressure radial distribution to preclude the ap-

pearance of the $m = 0$ sausage mode [5]

$$-\frac{\mathrm{d}\ln(p)}{\mathrm{d}\ln(r)} \leq \frac{4\Gamma}{2+\Gamma\beta} \tag{2.4}$$

Similar analysis can be performed for $m \geq 2$ to yield $= \frac{\mathrm{d}\ln(p)}{\mathrm{d}\ln(r)} < \frac{m^2}{\beta}$. Prior work by [6] has also shown that the $m = 1$ kink mode can be prevented with sufficient velocity shear, $\frac{\mathrm{d}V_z}{\mathrm{d}r} > 0.1kV_A$, in the presence of a conducting wall. More recent experimental and computational work has shown that the conducting wall is not necessary for stability [7].

2.2 Spectroscopy theory

We now turn to a description of the processes that produce the radiation of interest for spectroscopy. Although a plasma is capable of producing a wide range of radiation, its emission of line radiation, corresponding to the discrete transitions of bound electrons between energy levels, is most important for characterizing the plasma dynamics of the ZaP experiment. Although the line radiation measured by the spectroscopy system is exclusively from impurities, as hydrogen emission is burned through under ZaP run conditions, much of the referenced theory deals with hydrogen-like cases, which is to say electronic structures in which the transiting electron can be assumed to be free of electron-electron correlations. In the absence of significant electron-electron interactions, the wavefunction of the transiting electron is separable and its Hamiltonian can be expanded in a perturbation series, where the perturbation describes the effect of either collisions (the Stark effect) or a background magnetic field (Zeeman effect). This should prove to be a valid assumption for the isolated 2p electron transitions that produce the C IV line of interest.

What follows is a brief discussion of the three major line-altering mechanisms found in the ZaP plasma: The Zeeman splitting caused by the background magnetic field, the Doppler broadening due to a radiator's non-zero temperature, and the pressure (Stark) broadening due to electron-radiator collisions. Unsurprisingly, the measurement of these three effects then allow us to measure

the plasma's magnetic field, temperature, and electron density at the location of the radiator.

2.2.1 Zeeman splitting, the perturbation of a magnetic field

An intuitive approach to describing the effects of a magnetic field on the energy states of an electron is to think of the Hamiltonian as a description of the electron's energy. Then, if the magnetic field is small, its effect can be thought of as an energy perturbation to the background Hamiltonian. In this thesis we follow the development of Zeeman splitting as shown in [10]. If we consider the background Hamiltonian to be the typical summation of the electron's kinetic energy with the Coulomb potential supplied by a positively charged nucleus, the background Hamiltonian takes the form

$$\hat{H}_o = \frac{\hat{p}^2}{2\mu} - \frac{Ze^2}{|\hat{r}|}, \tag{2.5}$$

where $\hat{p}$ is the momentum operator, μ is the reduced mass of the electron and nucleus, Z is the effective charge of the nucleus (protons minus non-radiating electrons), e is the fundamental charge, and $\hat{r}$ is the position operator.

Electrons are charged and carry both intrinsic angular momentum from their spin and orbital state. In the classical analogue we could treat them as a current loop with some magnetic moment. The energy of this classical system would then be the scalar product of the electron's magnetic moment with the background magnetic field. In the quantum world, we do just this but through operator notation, where the perturbing Hamiltonian takes the form

$$\hat{H}_p = -\hat{\mu} \cdot \vec{B} = -\left(\frac{-e}{2m_e c}\hat{L} + \frac{-e}{m_e c}\hat{S}\right) \cdot \vec{B}, \tag{2.6}$$

where we have made use of the rather unfortunate confluence of nomenclature to refer to the magnetic moment of the electron as $\hat{\mu}$; in addition m_e is the mass of the electron, c is the speed of light, $\hat{L}$ is the angular momentum operator, $\hat{S}$ is the spin operator, and $\vec{B}$ is the magnetic field that's causing all this commotion.

We can then choose the magnetic field to align with the z direction and compute the expected value of this perturbation Hamiltonian to see how the energy level of an electron changes in the presence of a magnetic field.

$$E_{M_J} = \langle \mu \cdot B \rangle = g_J \frac{\mu_B B}{\hbar} = g_J \mu_B M_J B. \tag{2.7}$$

In the above g_J is the Landé factor and M_J are the eigenvalues of $\hat{J}_z$ reduced by a factor of $\hbar$, such that

$$M_J = J, J-1, ..., -J+1, -J \tag{2.8a}$$

$$g_J = 1 + \frac{J(J+1) + S(S+1) - L(L+1)}{2J(J+1)}. \tag{2.8b}$$

An example greatly clarifies the resulting energy splittings. Consider the C IV transition at 581.2 nm from a $^2P_{1/2}$ state to a $^2S_{1/2}$ state (we will use this line later on for our measurements of the ZaP-HD plasma). The procedure for any other line would be largely the same, with, of course, there being the potential to have more terms and different values for L, J, g, and M_J, as noted above. A qualitative overview of this transition is shown in Figure 2.1. The upper level has $L = 1$, $S = 1/2$, $J = 1/2$ and thus $g_J = 2/3$; it is split into $M_J = \{+1/2, -1/2\}$. If we let the unperturbed initial state be $E_{unperturbed,\,i} = E_{o,\,i}$, then we can describe the resulting energy levels of the initial state in the presence of a magnetic field as: $E_i = E_{o,\,i} + g_J \mu_B \{M_J\} B = E_{o,\,i} + g_J \mu_B B \{+1/2,\ -1/2\}$. Likewise, the lower level is split according to $E_f = E_{o,\,f} = g_J \mu_B \{M_J\} B = E_{o,\,i} + g_J \mu_B B \{+1/2,\ -1/2\}$. Noting that the selection rule that $\Delta M = 0, \pm 1$ for an allowed dipole transition is satisfied by each of the four permutations of initial and final energy levels and that the change in energy of the transition will be the energy change of the top state minus the energy change of the bottom state leads to the following changes to the energy of the emitted photon:

$M_J : +1/2(\text{high state}) \rightarrow +1/2(\text{low state})$

$$\Delta E_{+1/2\to+1/2} = -2\mu_B B(1/2) + (2/3)\mu_B B(1/2) = -2/3\mu_B B.$$

$$M_J : +1/2 \to -1/2$$

$$\Delta E_{+1/2\to-1/2} = -2\mu_B B(1/2) - (2/3)\mu_B B(1/2) = -4/3\mu_B B.$$

$$M_J : -1/2 \to +1/2$$

$$\Delta E_{-1/2\to+1/2} = -2\mu_B B(-1/2) + (2/3)\mu_B B(1/2) = 4/3\mu_B B.$$

$$M_J : -1/2 \to -1/2$$

$$\Delta E_{-1/2\to-1/2} = -2\mu_B B(-1/2) - (2/3)\mu_B B(1/2) = 2/3\mu_B B.$$

The first and fourth transition listed above are transitions for which M_J does not change. For the second and third transitions M_J changes as -1 and $+1$ respectively. Conservation of angular momentum, in conjunction with the unitary spin of a photon, reveals that the photons emitted from these transitions will be entirely right-hand circularly-polarized (RHP) when $\Delta M_J = 1$ and entirely left-hand circularly-polarized (LHP) when $\Delta M_J = -1$. For the case that $\Delta M_J = 0$, the light is unpolarized. Fortunately, the alignment of our line of sight with the magnetic field will prevent us form observing the $\Delta M_J = 0$ transitions. Furthermore, we can rewrite the change in energy as a change in wavelength by noting that $E = hc/\lambda$, differentiating with respect to λ, and rearranging to arrive at the equation,

$$\Delta\lambda = \mu_B B \Delta(Mg)\lambda_o^2, \tag{2.9}$$

where $\Delta(M_J g)$ is the difference of the product of M_J and g for the lower and upper state and λ_o is the unshifted wavelength [9].

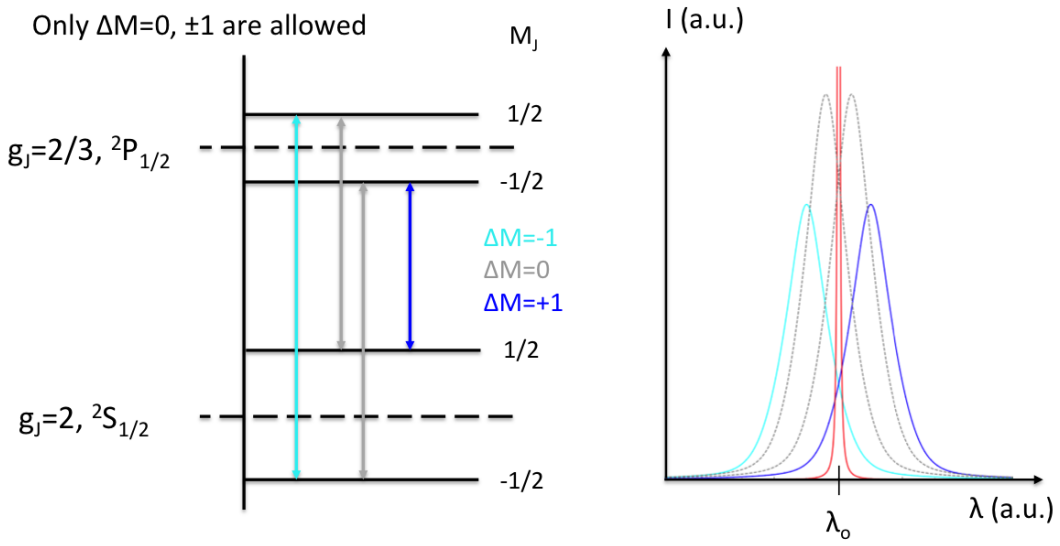

Figure 2.1 An energy level diagram (left) and resulting line emission profile (right) are shown for the C IV transition at 581.2 nm. The energy level diagram shows the qualitative dependence of energy on magnetic quantum number, M_J, when an external magnetic field is applied. The transitions are colored according to the change in M_J. Cyan is $\Delta M_J = -1$; Gray is $\Delta M_J = 0$; Blue is $\Delta M_J = +1$. The qualitative effect of this fine structure on the emitted spectrum is shown in the line emission profiles to the right, with temperature and pressure broadening also included. The red curve is the natural line, i.e., the spectrum without magnetic field, temperature, or pressure effects. The four other curves demonstrate these effects and are colored according to their change in M_J.

2.2.2 Doppler broadening

If the radiator is of non-zero but non-relativistic temperature and in local thermodynamic equilibrium, then the line radiation also takes on the form of a Gaussian. For a wave with velocity along the line of sight of a stationary observer, the Doppler shift is described by

$$\lambda = \lambda_o \left(1 - \frac{\hat{s} \cdot \vec{v}}{c}\right), \tag{2.10}$$

where λ_o is the unshifted wavelength, $\hat{s}$ is the line of sight of the observer, $\vec{v}$ is the source's velocity, and c is the speed of light. We can then consider the wavelength distribution for a small volume of

plasma with a Maxwellian velocity distribution to also be normally distributed.

$$G[\lambda] \propto \exp\left[-\frac{m_i c^2}{2kT_i\lambda_o}\right], \tag{2.11}$$

where m_i is the mass of the radiator, k is Boltzmann's constant, and T_i is the ion temperature. In this way, measuring the spectral profile of a line transition and its Full Width at Half the Maximum (FWHM) determines the temperature of the radiating volume of plasma.

2.2.3 Stark broadening

For cases when the collisions are of characteristic times smaller than the natural decay time of an excited state, Stark broadening can be described through the impact approximation [12]. This translates to the requirement that $v/\rho >> sup(|\Delta\omega|, w)$, where v is the characteristic velocity of the collision, ρ is the impact parameter of the collision, $\Delta\omega$ is the smallest frequency resolution of the Fourier integral of the desired line profile, and w is the half-width of the line profile. It is assumed that this condition is satisfied by the ZaP-HD plasma. It is shown in [13] that the resulting-line broadened profile takes the form

$$L(\omega) = \frac{w/\pi}{w^2 + (\Delta\omega - d)^2}, \tag{2.12}$$

where w is the half width at half the maximum and d is the shift (for our purposes d will be the centroid of the line). Assuming that the Stark perturbation frequencies are small compared to their unperturbed values, the above frequency variables can be converted into wavelength space through the difference approximation of the derivative of $\lambda = 2\pi c/\omega$, such that $w(\lambda) = w(\omega)\lambda_o^2/2\pi c$ and $d(\lambda) = -d(\omega)\lambda_o^2/2\pi c$. A more complete discussion of Stark broadening can be found in [12] with additional nuggets in [13] and [14]. Applying these conversions, as seen in [15], yields the Lorentzian,

$$L(\omega) = A_L \frac{W_L^2}{4(\lambda - \lambda_o)^2 + W_L^2}, \tag{2.13}$$

where we allow for some amplitude scaling with the term A_L and use the FWHM, W_L, in place of the HWHM used before.

2.2.4 The combined effect of temperature and pressure broadening

In the ZaP-HD experiment the collisions that cause pressure broadening and the collisions that enforce local thermodynamic equilibrium (LTE) are expected to be statistically independent as electron-ion collisions contribute to pressure broadening, while ion-ion collisions enforce LTE; for cases when the two collisions are not independent the reader is directed to [11]. Thus, the resulting line emission profile is the convolution of the Gaussian and Lorentzian profiles mentioned previously; such a profile is known as a Voigt profile.

$$V[\lambda] = G[\lambda] * L[\lambda] = \int_{-\infty}^{+\infty} A_G \exp\left[-\frac{4\ln(2)(\tau_1-\lambda_o)^2}{W_G^2}\right] A_L \frac{W_L^2}{4(\tau_1-\lambda_o)^2+W_L^2} \mathrm{d}\tau_1, \qquad (2.14)$$

where A_G and A_L are the respective amplitudes of the Gaussian and Lorentzian components, τ_1 is the dummy variable of convolution, and W_G and W_L are the respective FWHMs. A comparison between Gaussian, Lorentzian, and Voigt profiles can be seen in Figure 2.2 for the case that each profile is normalized to have an area of one. The Gaussian profile dominates close to the center of the profile, while the Lorentzian dominates in the wings. The Voigt profile is broader than either the Gaussian or the Lorentzian.

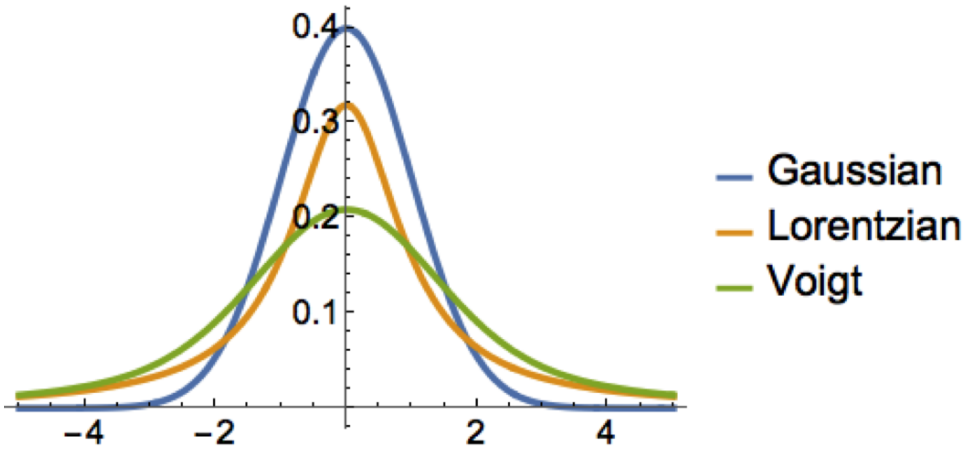

Figure 2.2 The relative shape of a Gaussian (cobalt), Lorentzian (citrine), and Voigt (avocado) profiles. Each has been normalized to have an area of one. The Voigt profile is the convolution of the Gaussian and Lorentzian. The Gaussian dominates near to the origin, while the Lorentzian dominates in the wings.

Chapter 3

Experimental Set Up and Telescope Redesign

The ZaP-HD Z-pinch plasma sits within a cylindrical vacuum chamber. Rectangular quartz windows offer optical access to the plasma. In order for the spectrometer to provide spatial resolution of the Z-pinch, a telescope reimages the plasma onto a fiber bundle that then carries the light to the spectrometer. This section will describe this set up and the redesign of the telescope for 1:1 magnification of the plasma.

3.1 An overview of the spectroscopy system

The hardware of the spectroscopy system funnels light emitted from the plasma to the spectrometer, where it is splayed out according to wavelength. There are several pieces to this system, a summary of which can be seen in Figure 3.1. The first is the telescope that reimages light emitted from the plasma onto a fiber bundle. The telescope presently on the ZaP-HD experiment has a magnification of -0.5x. A new telescope with magnification 1.0x was designed for future use on the ZaP-HD experiment; this design is documented in section 3.2. For Zeeman spectroscopy the fiber bundle is

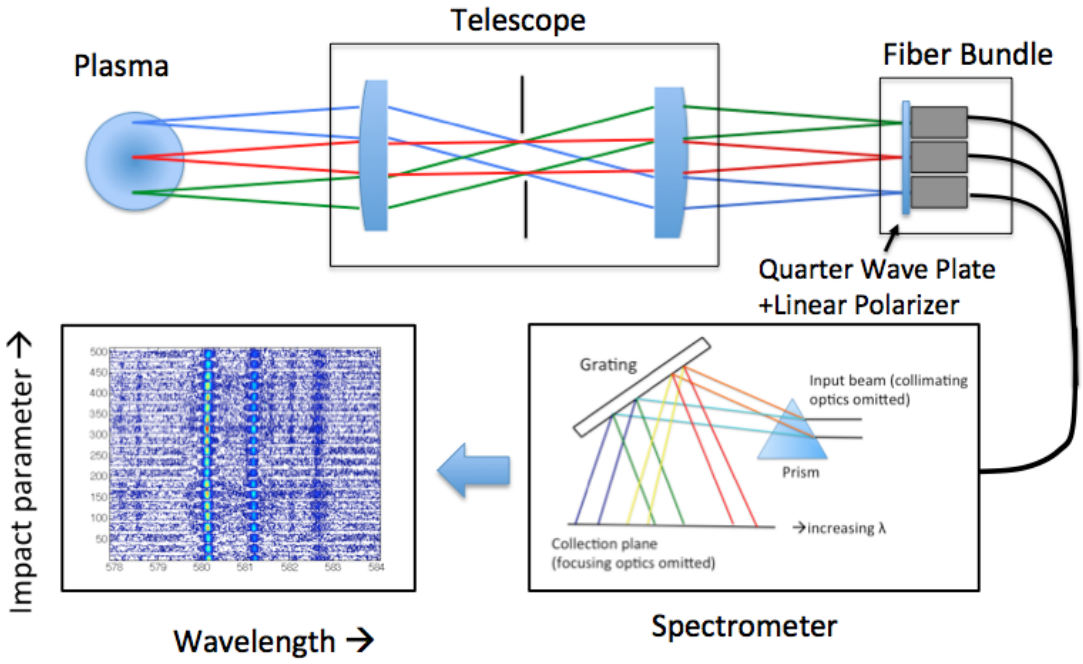

Figure 3.1 An overview of the spectroscopy system: Light is emitted from the plasma and is reimaged by a telecentric telescope onto a fiber bundle. The fiber bundle is preceded by a linear polarizer and quarter wave plate to separate right-hand circularly-polarized light from left-hand circularly-polarized light. The fiber bundle then ferries the light to the spectrometer, which outputs a 512×512 array of pixel intensities.

split into two stacks that view the plasma at the same impact parameters. One stack receives the left-hand circularly-polarized (LHP) light while the other stack receives the right-hand circularly-polarized (RHP) light, as seen in Figure 3.2. The difference in centroid position between the stacks depends linearly on the magnetic field.

The light is separated into polarization states by preceding the fiber bundle with first a linear polarizer and then a quarter-wave plate (QWP), as documented in [17]. Furthermore, because the line of sight of the telescope is parallel with the magnetic field, only the σ components, which correspond to transitions of $\Delta M_J = \pm 1$, are observed (ignoring the contamination due to the outer shells of the plasma). Thus, the QWP takes in LHP light and RHP light and returns linearly

polarized light at an angle with respect to the fast axis of the QWP of -45° for RHP light and $+45^\circ$ for LHP light. Because the QWP is oriented with its fast axis at 45° to the machine axis, the resulting angles with respect to the machine axis are 0° and 90°, i.e. parallel and perpendicular to the machine axis. The subsequent linear polarizers, one of which is oriented along the machine axis, while the other is oriented perpendicular to it, then filter out the unwanted polarization state, leaving only RHP light for one fiber stack and LHP light for the other.

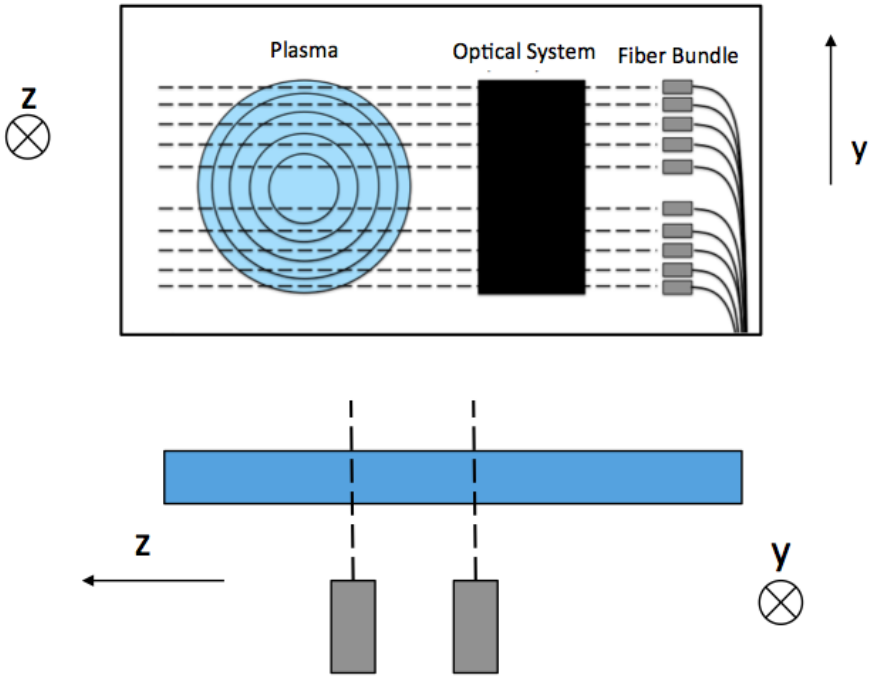

Figure 3.2 The fiber bundle is split into two stacks of ten fibers each. Top: The ten fibers within a stack collect light cylinders that view the plasma at constant impact parameter. Bottom: The two stacks allow for one stack to collect only left-hand circularly-polarized light while the other collect only right-hand circularly-polarized light. The two stacks are offset from another by 6.2 mm in the z direction.

3.2 Telescope redesign

The original radial and oblique telescopes on the ZaP-HD experiment provided telecentric and blurless imaging for plasmas within $\pm$ 10 mm of the nominal object plane of the telescope with a magnification of -0.5x. The design of this telescope was described in [16]. ZaP-HD, though, is expected to produce a pinch much smaller in radius than ZaP. Thus, the telescope was redesigned to provide a magnification of 1.0x while maintaining its telecentric and blurless imaging with a depth of field of $\pm$ 10 mm. In order to shorten the length of the telescope, a three-lens design was selected for both the radial and oblique telescopes. This three-lens design allows two longer focal length lenses to be combined to achieve a shorter focal length than could be provided by off-the-shelf components from major manufacturers. The optical design was conducted in Zemax Optical Design Software guided by some ray transfer matrix analysis for ideal lenses. The characteristic distances of the final design can be seen below in Figure 3.3 and Figure 3.4. The remainder of this section describes this process and the resulting system.

The design process began in the paraxial limit, i.e., ray bundles are sufficiently small in angular extent such that in Snell's Law $\sin\theta \approx \theta$. The goal was to produce the shortest telescope while maintaining a telecentric and blurless system. The limiting factor was the availability of lenses of sufficient diameter and focal length. The lenses were chosen from the off-the-shelf plano-convex optics offered by Thorlabs, Newport, Edmunds, and CVI. As a first order design the lenses were selected according to a paraxial model of system performance. Zemax was then used to determine the iris size and optimal focal plane. In Zemax, the system was initially designed for the 229.7 nm line. This is in part because 229.7 nm is the brightest line observed (and thus the best for velocity-shear measurements) but also because optical systems are more sensitive to aberration at smaller wavelengths; the wavelength dependence on the index of refraction in essence reduces the power of a lens at longer wavelength and, in so doing, reduces its contribution to wavefront error. The iris' location and size and the position of the final focal plane were then determined for wavelengths of

380 nm and 581 nm.

The minimum focal length of the first lens is set by the distance from the center of the machine to the surface of the carriage where the telescope is mounted. For the radial telescope, this is a distance of around 250 mm. For the oblique telescope, this is a distance of around 400 mm; off-the-shelf lenses are only offered in increments of 50 mm. The first lens collimates the diverging light coming from the plasma and forms a pupil plane one focal length from the first lens. For the telescope to be telecentric, the system's aperture must be placed at the pupil plane. A telecentric system reimages the object out to infinity (as viewed from the image plane), and thus motions of the object away from the object plane do not alter the centroid's position in the image plane.

However, the shell model used to analyze the Z-pinch requires that light emitted from one chord (impact parameter) cannot contaminate another chord. This equates to a restriction on the angular extent of the diverging ray bundle coming from a point on the object, such that for motions of the plasma within $\pm$ 10 mm the spot size in the image plane does not exceed the distance between fibers. This required the iris to be stopped down to an even smaller diameter. The diameter was determined such that for an on-axis source (aligned with the optical axis of the lenses) and an off-axis source (offset in the transverse direction from the optical axis) the radial extent of a source in the image plane never exceeded 250 μm for plasma motion of $\pm$ 10 mm.

In Zemax, the radial extent of point on the object in image space can be graphed using an encircled energy plot. Encircled energy plots show the fractional intensity of light, referenced to the amount of light exiting the system's aperture (the iris), as a function of distance to the centroid of the ray bundle. Encircled energy plots for the final radial and oblique telescopes are shown in Figure 3.5 and Figure 3.6 for 229.7 nm light with an iris diameter of 10 mm for the radial telescope and 16 mm for the oblique telescope. The encircled energy plots for the radial and oblique telescopes at 380 nm and 581 nm are shown at the end of this section in Figures 3.9 — 3.12. With each set of encircled energy plots is a spot diagram that qualitatively demonstrates

image quality. A spot diagram, much like a Poincaré section, traces rays from a source on the object through the system to the intersection of the ray with the image plane.

In order to achieve 1.0x magnification the second and third lens must have an equivalent focal length to the first lens. An equivalent ideal lens, in the small angle approximation, can be constructed according to the equation

$$\frac{1}{f_{eq}} = \frac{1}{f_1} + \frac{1}{f_2} - \frac{d}{f_1 f_2} = \frac{f_1 f_2}{f_1 + f_2 - d}, \tag{3.1}$$

where f_1 is the focal length of the first lens, f_2 is the focal length of the second lens, and d is the distance between the two lenses. Furthermore, ray tracing matrix analysis can be used to determine the distance between the object plane and lens 1, lens 1 and lens 2, and lens 2 and the image plane. In the paraxial limit, matrices can be constructed to describe the evolution of a ray bundle through an optical system. Working in a two-dimensional space (the lenses of interest are rotationally symmetric about the optical axis) and setting the optical axis as the z direction, a ray can be defined by the vector $[x, \theta]$, where x is the height of a ray and θ is its angle. Propagation through free space can be described by the matrix operator $\begin{bmatrix} 1 & d \\ 0 & 1 \end{bmatrix}$, where d is the distance along the optical axis of propagation. Refraction at a thin lens is described by $\begin{bmatrix} 1 & 0 \\ -\frac{1}{f} & 1 \end{bmatrix}$.

Thus to determine the distances between two lenses equivalent to a one lens system of known focal length the following system can be solved,

$$\begin{bmatrix} 1 & t3 \\ 0 & 1 \end{bmatrix} \begin{bmatrix} 1 & 0 \\ -\phi_2 & 1 \end{bmatrix} \begin{bmatrix} 1 & t2 \\ 0 & 1 \end{bmatrix} \begin{bmatrix} 1 & 0 \\ -\phi_1 & 1 \end{bmatrix} \begin{bmatrix} 1 & t1 \\ 0 & 1 \end{bmatrix} = \begin{bmatrix} 1 & 1/\phi_3 \\ 0 & 1 \end{bmatrix} \begin{bmatrix} -1 & 0 \\ -\phi_3 & 1 \end{bmatrix} \begin{bmatrix} 1 & 1/\phi_3 \\ 0 & 1 \end{bmatrix}, \tag{3.2}$$

where ϕ_i is the power of lens i (one over the focal length), t_1 is the distance from the object to the first lens, t_2 is the distance from lens 1 to lens 2, t_3 is the distance from lens 2 to the image plane lens i to the next lens. For the single lens, the distance from the image plane to the lens is $1/\phi_3 = f_3$, where f_3 is the focal length of the equivalent lens. Because the two lenses that

comprise the equivalent lens are of equal focal length, the distances must be symmetric. Thus, $t_3 = t_1$ and the system is solvable. The two values of t_1 and t_2 were passed to the Zemax design. The final distance was optimized in Zemax to minimize spot radius. The final design prescriptions can be seen below in Figure 3.7a and Figure 3.8a while the ray diagrams can be seen in Figure 3.7b and Figure 3.8b. The iris dimension and position along with the focal position for the three characteristic wavelengths of 229 nm, 380 nm, and 581 nm are shown in Figures 3.3 and 3.4.

Wavelength	Distance from First Lens to Iris	Iris Semi-Diameter	Distance from Third Lens to Focal Plane
227 nm	250.31 mm	5 mm	34.07 mm
380 nm	276.91 mm	5 mm	81.47 mm
581 nm	285.13 mm	5 mm	94.62 mm

Figure 3.3 The size and location of the iris and the focal plane of the radial telescope. All distances are measured to the nearest surface of the reference component.

Wavelength	Distance from First Lens to Iris	Iris Semi-diameter	Distance from Third Lens to Focal Plane
227 nm	394.22 mm	8 mm	93.13 mm
380 nm	435.99 mm	10 mm	165.10 mm
581 nm	449.10mm	10 mm	186.15 mm

Figure 3.4 The size and location of the iris and the focal plane of the oblique telescope. All distances are measured to the nearest surface of the reference component.

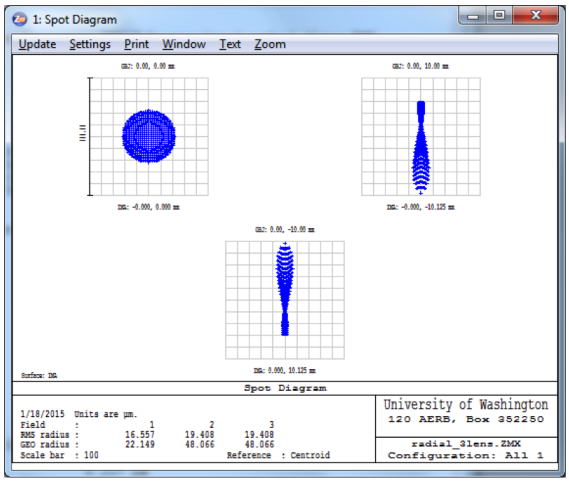

(a) A spot diagram shows the images of an on-axis and two off-axis sources (± 10 mm) when the object plane is in focus.

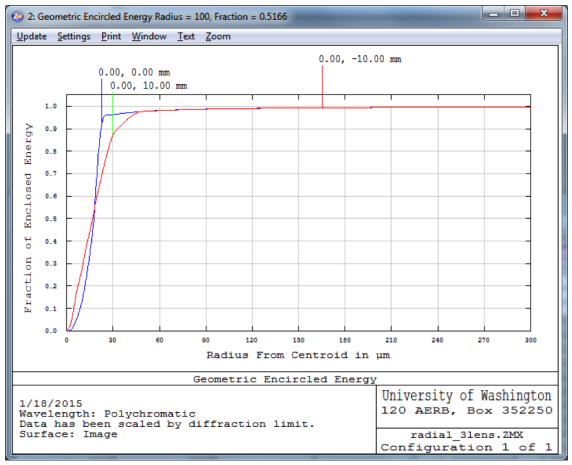

(b) An encircled energy plot with the object plane located at the focal plane of the first lens.

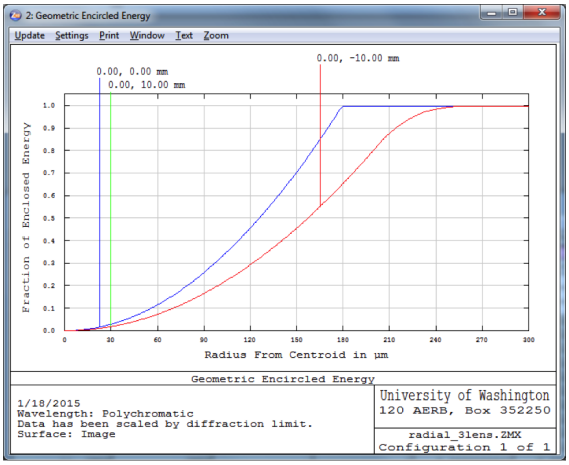

(c) An encircled energy plot with the object plane located 10 mm farther from the focal plane of the first lens.

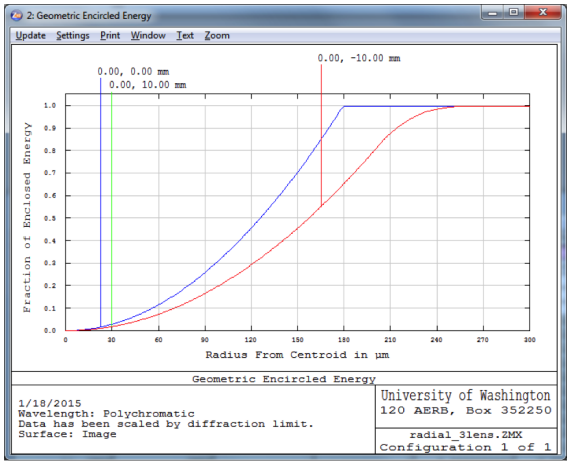

(d) An encircled energy plot with the object plane located 10 mm closer to the focal plane of the first lens.

Figure 3.5 A spot diagram with encircled energy plots for the radial telescope operating at 229.7 nm. Rays originating from three positions in object space are propagated through the system and the fractional extent, referenced to the centroid of the ray bundle, of the spot size in the image plane is calculated. The full extent of the bundle is referenced to the size of the ray bundle passing through the system's aperture (the iris). The spot diagram for the focused case is shown to demonstrate the expected geometric aberrations introduced for off-axis sources.

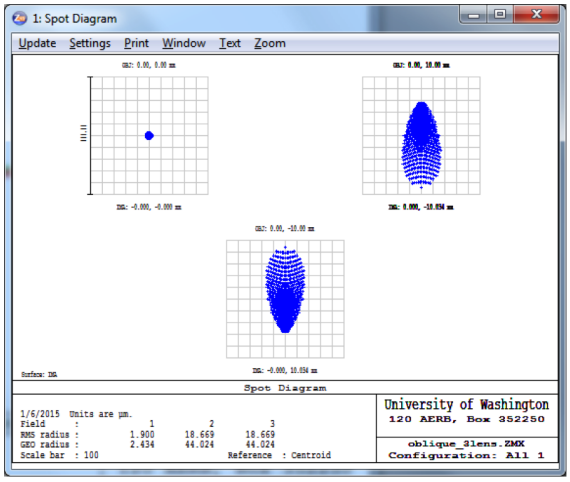

(a) A spot diagram shows the images of an on-axis and two off-axis sources ($\pm$10 mm) when the object plane is in focus.

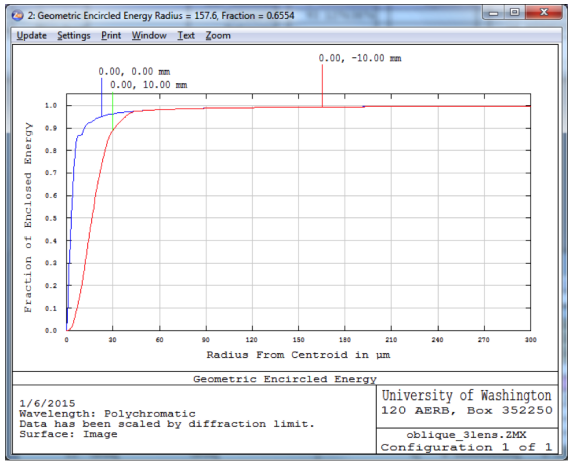

(b) An encircled energy plot with the object plane located at the focal plane of the first lens.

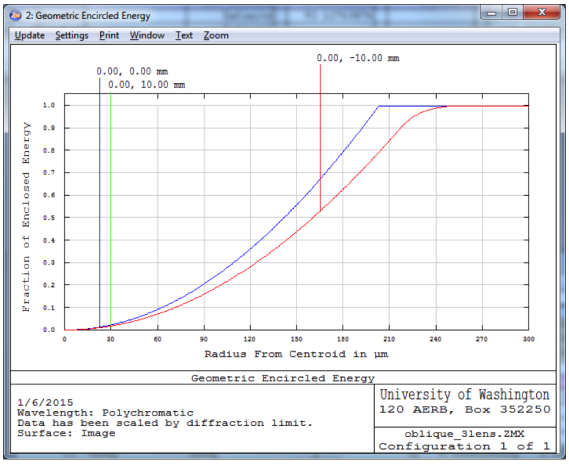

(c) An encircled energy plot with the object plane located 10 mm farther from the focal plane of the first lens.

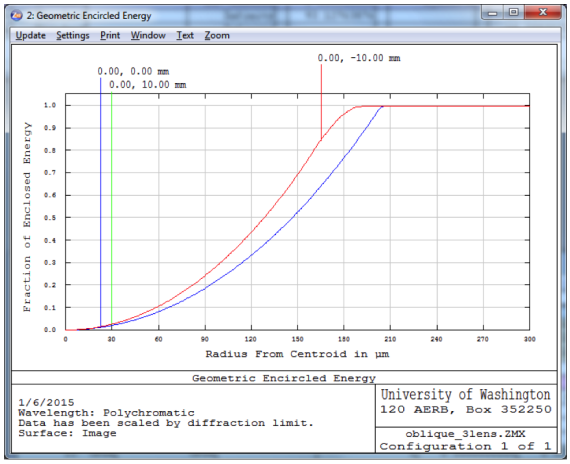

(d) An encircled energy plot with the object plane located 10 mm closer to the focal plane of the first lens.

Figure 3.6 A spot diagram with encircled energy plots for the oblique telescope operating at 229.7 nm. Rays originating from three positions in object space are propagated through the system and the fractional extent, referenced to the centroid of the ray bundle, of the spot size in the image plane is calculated. The full extent of the bundle is referenced to the size of the ray bundle passing through the system's aperture (the iris). The spot diagram for the focused case is shown to demonstrate the expected geometric aberrations introduced for off-axis sources.

	Focal Length (mm)	Radius of Curvature (mm)	Semi-Diameter (mm)	Material	Supplier
Lens 1	254	130.8	50.8	Fused Silica	CVI
Lens 2	300	154.5	50.8	Fused Silica	CVI
Lens 3	300	154.5	50.8	Fused Silica	CVI

(a) The lens prescriptions for the radial telescope

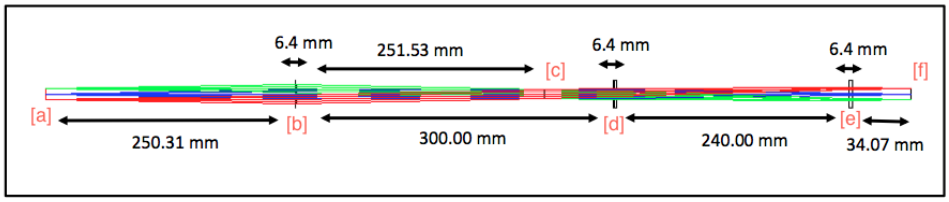

(b) A ray diagram of the radial telescope shows the position of all three lenses, the position of the iris, and the relevant distances (all for a wavelength of 229.7 nm). From [a] light is emitted from three point sources located at impact parameters of +10 mm (green), 0 mm (blue), and -10 mm (red). At [b] a 250 mm focal length lens collimates the light to form a pupil plane at [c], where the iris is located. Lenses at [d] (fl=300 mm) and [e] (fl=300 mm) focus the collimated light to form an image plane at [f].

Figure 3.7 An overview of the radial telescope design

	Focal Length (mm)	Radius of Curvature (mm)	Semi-Diameter (mm)	Material	Supplier
Lens 1	400	206	50.8	Fused Silica	CVI
Lens 2	500	257.5	50.8	Fused Silica	CVI
Lens 3	500	257.5	50.8	Fused Silica	CVI

(a) The lens prescriptions for the radial telescope

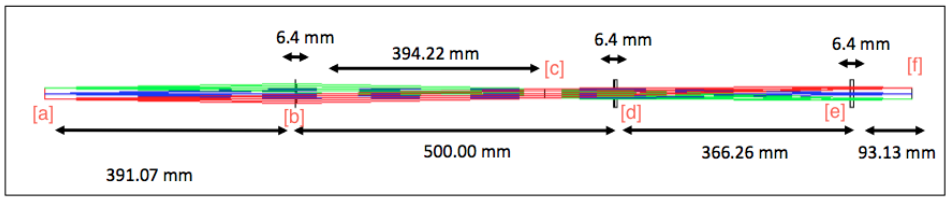

(b) A ray diagram of the oblique telescope shows the position of all three lenses, the position of the iris, and the relevant distances (all for a wavelength of 229.7 nm). From [a] light is emitted from three point sources located at impact parameters of +10 mm (green), 0 mm (blue), and -10 mm (red). At [b] a 400 mm focal length lens collimates the light to form a pupil plane at [c], where the iris is located. Lenses at [d] (fl=500 mm) and [e] (fl=500 mm) focus the collimated light to form an image plane at [f].

Figure 3.8 An overview of the oblique telescope design

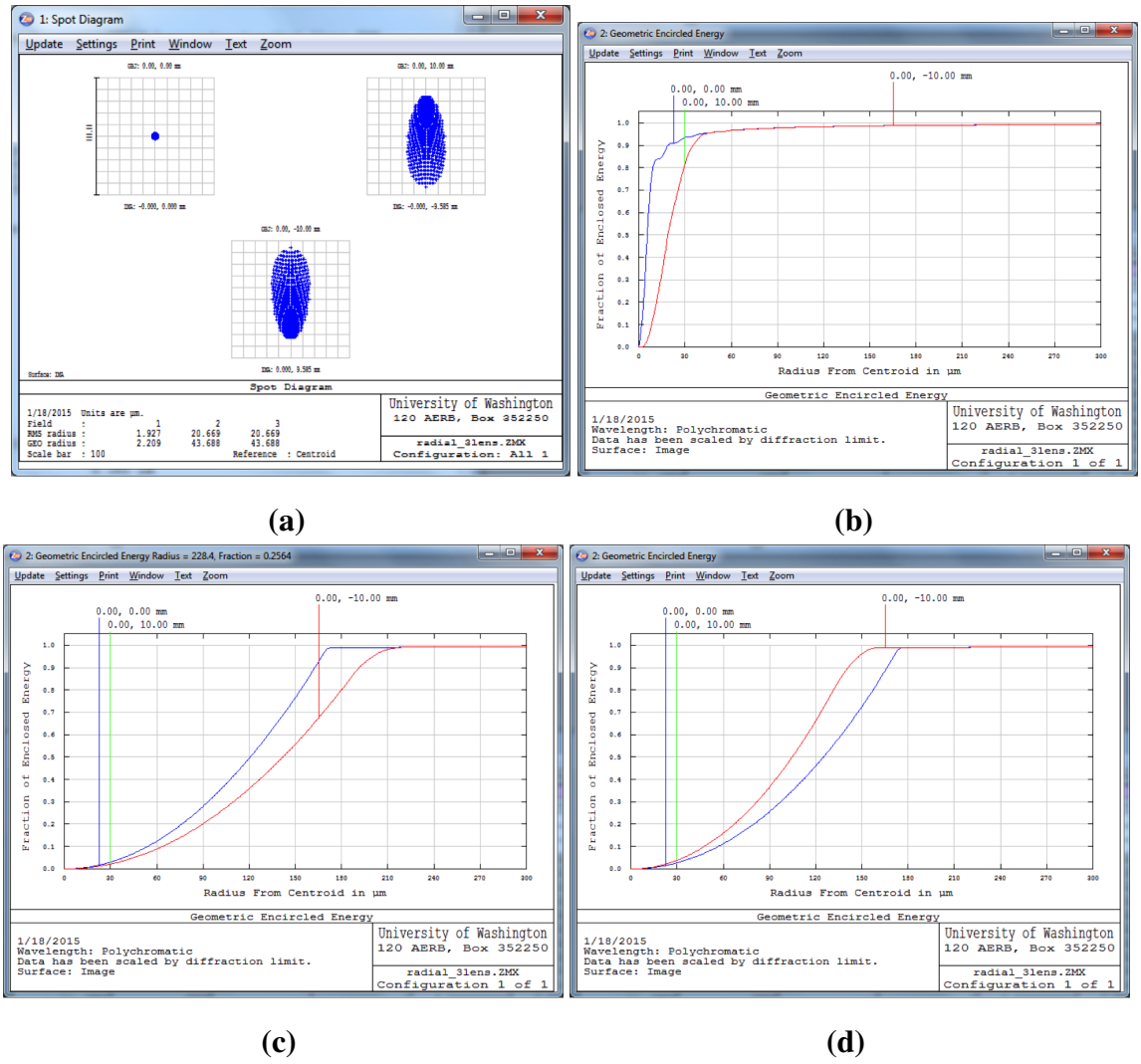

Figure 3.9 The performance of the radial telescope at 380 nm.

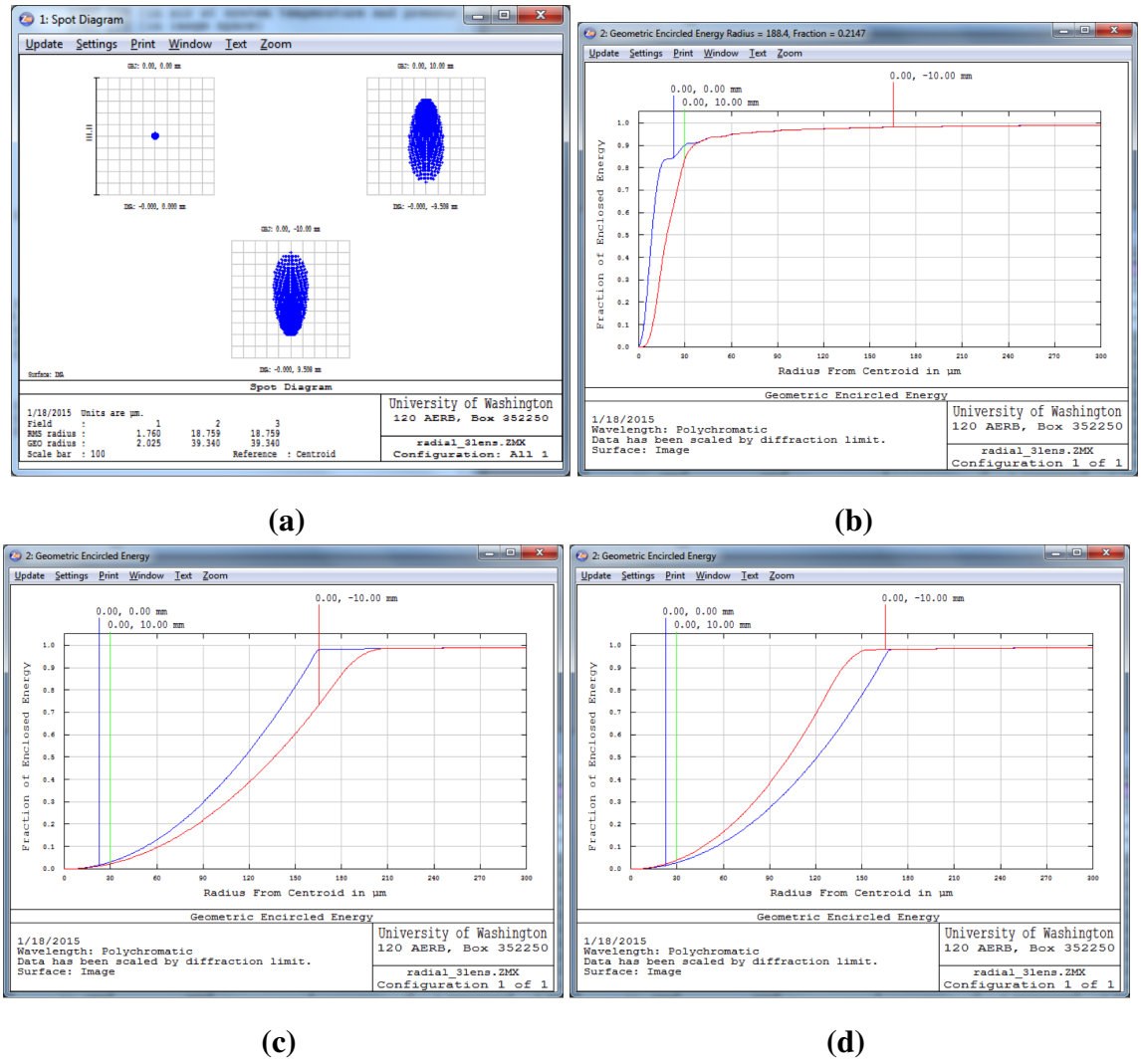

Figure 3.10 The performance of the radial telescope at 581 nm.

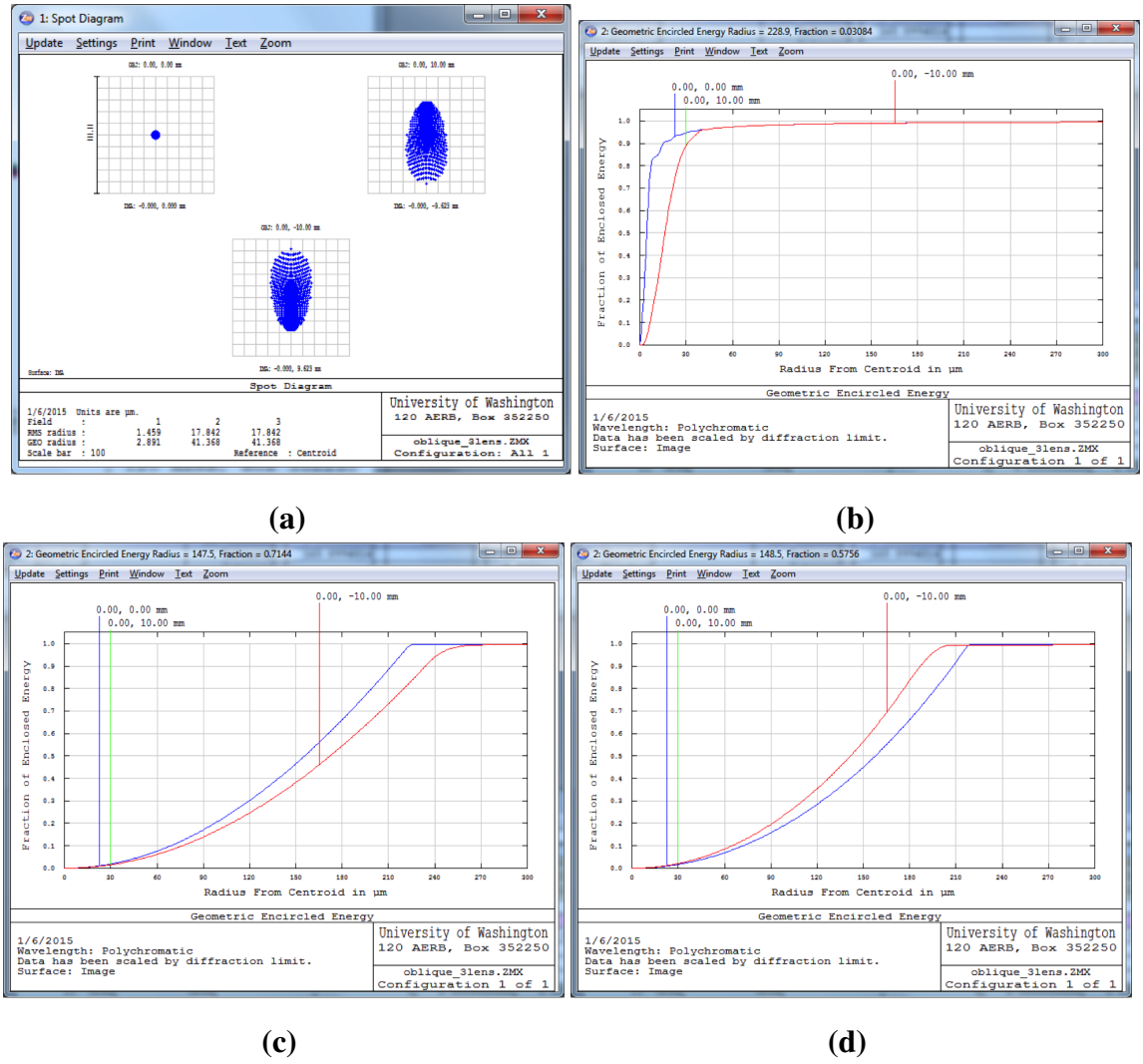

Figure 3.11 The performance of the oblique telescope at 380 nm.

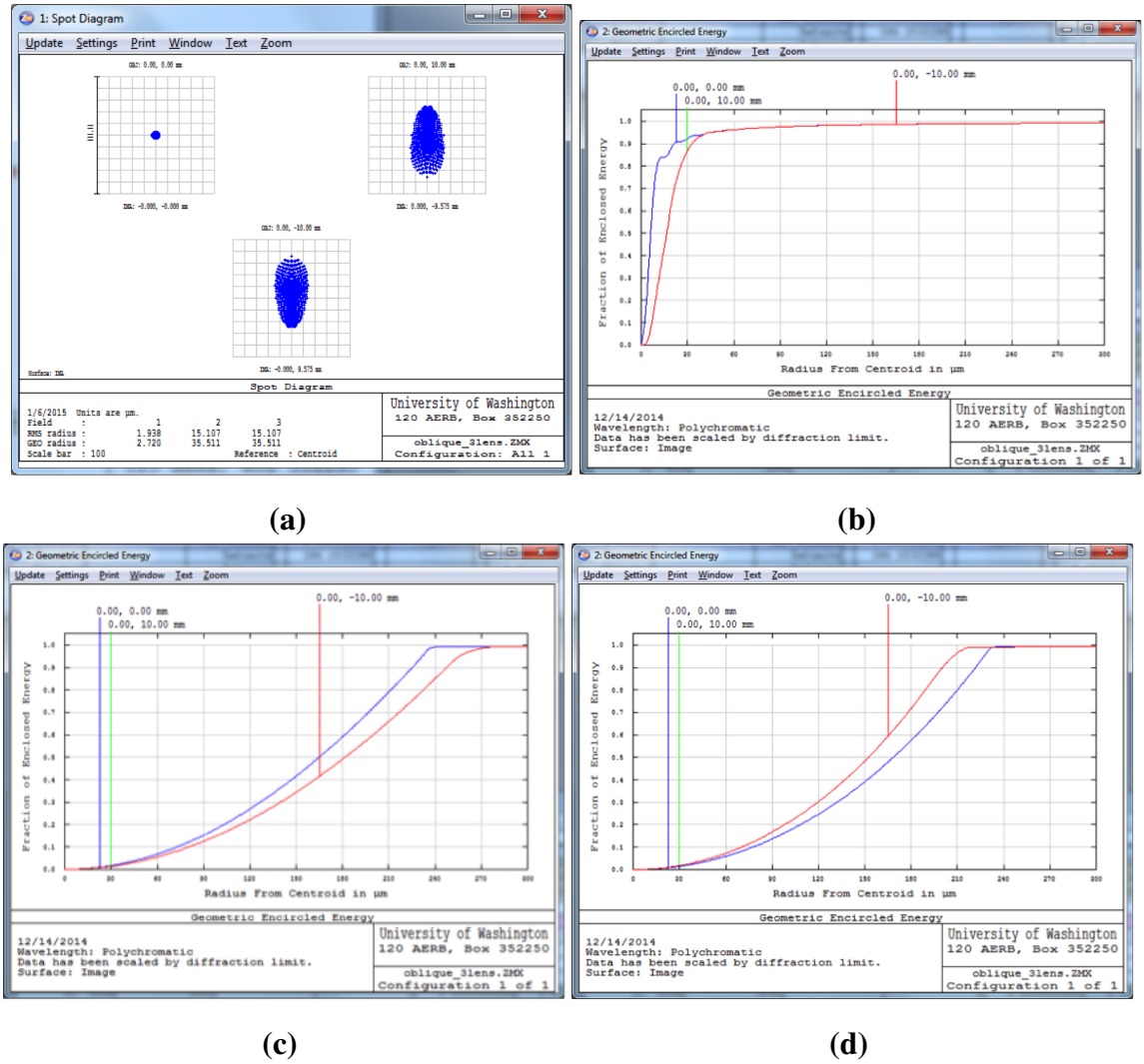

Figure 3.12 The performance of the oblique telescope at 581 nm.

Chapter 4

Data Analysis

In this section we turn to the data analysis procedure beginning with an overview of the Fourier fitting process. The second part of this section deals with the sensitivity analysis of the code, quantifying the code's ability to simultaneously resolve temperature and electron density over a parameter space representative of recent data and with varying amounts of noise added. The final part shows the results from a data set with sufficiently small noise levels.

4.1 Fourier transform fitting

As was discussed in section 2, there are three line-altering mechanisms of interest. The first is the Doppler broadening due to thermal motion. The second is the pressure broadening due to fast perturbations on the excited radiator. The third is the fine structure splitting due to the background magnetic field. Thus, the final data set is a convolution of these three mechanisms with the instrument function inherent to the detector. The convolution of two functions is defined as,

$$f(x) * g(x) = \int_{-\infty}^{+\infty} f(\tau) g(x-\tau) \mathrm{d}\tau. \tag{4.1}$$

Convolution is commutative, associative, distributive, and for our purposes supports the identity relation, $f * \delta = f$, where δ is the Dirac delta function (this last property is why we can ignore natural broadening in our treatment). Under a Fourier transformation, the convolution of two functions reduces to multiplication, i.e. $F[f(x) * g(x)] = f(k)g(k)$.

In the absence of noise, a single transition captured by the spectrometer would be the convolution of the Doppler broadening's Gaussian function, the Stark broadening's Lorentzian, and the instrument function.

$$G[\lambda] * L[\lambda] * \text{Inst}[\lambda] = \int_{-\infty}^{+\infty} \left(\int_{-\infty}^{+\infty} G[\tau_1] L[\tau_2 - \tau_1] \mathrm{d}\tau_1 \right) \text{Inst}[\lambda - \tau_2] \mathrm{d}\tau_2, \tag{4.2}$$

where $G[\lambda] = A_G \exp[-\frac{4\ln 2(\lambda-\lambda_o)^2}{W_G^2}]$, $L[\lambda] = A_L \frac{W_L^2}{4(\lambda-\lambda_o)^2+W_L^2}$, and τ_i are dummy variables of integration (the W_i are the respective FWHMs). However, in Fourier space the above reduces to:

$$F[G[\lambda] * L[\lambda] * \text{Inst}[\lambda]] = G[k]L[k]\text{Inst}[k] = \text{Inst}[k] A_\nu \exp\left[-\frac{W_G^2 k^2}{16\ln 2} - \frac{W_L |k|}{2} \right] \tag{4.3}$$

This great reduction in complexity should then translate into superior fits. The fitting method was implemented in Matlab. The Fourier transform was supplied by a Cooley-Tukey Fast Fourier Transform (FFT). The least-squares (LSQ) fit was provided by Matlab's default 'Trust-Region-Reflective' algorithm.

Although the FFT LSQ fitter should provide a more direct path for resolving temperature and density, it does so at the cost of accessing the centroid of the profile. The original goal was to find the centroid of an emission profile through the phase of the Fourier spectrum. For the continuous Fourier transform the translation of the Voigt profile away from the origin results in a phase offset in Fourier space. More explicitly,

$$F[G[x-x_o]L[x-x_o]] = F[G[x-x_o]]F[L[x-x_o]] \tag{4.4a}$$

$$= e^{ix_o k - W_G^2 k^2/(16\ln 2)} e^{ix_o k - W_L|k|/2} \tag{4.4b}$$

$$= e^{i2x_o k} e^{-W_G^2 k^2/(16\ln 2) - W_L|k|/2.} \tag{4.4c}$$

The above can be thought of in phaser notation as the complex number $z = a + ib = re^{i\theta}$. By calculating $\theta = \mathrm{Tan}^{-1}[b/a]$ for a particular wavenumber, k, the offset can be determined. However in the discrete case no such algebraic process was found. Let us consider one point in our Fourier spectrum of length N

$$X[k] = \sum_{n=0}^{N-1} x_n e^{-2\pi ikn/N}. \tag{4.5}$$

Writing this out explicitly yields:

$$X[k] = x_0 e^0 + x_1 e^{-2\pi ik/N} + x_2 e^{-2\pi i2k/N} + ...x_{N-1} e^{-2\pi ik(N-1)/N}, \tag{4.6}$$

where each $x_i = \int_{-\infty}^{+\infty}(\int_{-\infty}^{+\infty} G[\tau_1]L[\tau_2 - \tau_1]\mathrm{d}\tau_1)\mathrm{Inst}[x_i - \tau_2]\mathrm{d}\tau_2$.

Noting Euler's identity, $e^{i\theta} = \cos[\theta] + i\sin[\theta]$, in order to separate real and imaginary parts in the above, the angle of a point in the Fourier spectrum can be calculated as

$$\theta[k] = \mathrm{Tan}^{-1}\left(\frac{x_1 \sin[-2\pi k/N] + ... + x_{N-1}\sin[-2\pi(N-1)k/N}{x_0\cos[0] + x_1\cos[-2\pi k/N] + ... + x_{N-1}\cos[-2\pi(N-1)k/N]}\right). \tag{4.7}$$

The above is transcendental and does not allow for a simple determination of x_{offset} under the translation $x_i = x + x_{\mathrm{offset}}$. Thus a regular (non-Fourier) LSQ method was also implemented to determine the centroid of an emission profile. However, this non-Fourier LSQ fit did not include the instrument function.

4.2 Software sensitivity analysis

The FFT LSQ fitter was first tested with synthetic data with known temperatures and electron densities to determine its ability to resolve temperature and density over a parameter range commonly found under experimental conditions. The data were constructed in wavelength space (non-Fourier space) spanning 512 pixels with equal spacing of 0.012 nm/pixel centered on the known centroid of the CIV line at 581.20 nm (technically the peak was located at pixel 257). This attention to pixel

spacing and peak location was to minimize spectral leakage due to the non-periodicity of the profile, as well as to prevent Matlab from initiating any interpolation scheme. This set up is simpler than the actual images recorded by the spectrometer, which do not have equal interpixel spacing. However, this sensitivity analysis was run under optimal conditions to distinguish between fundamental resolution limits and higher order effects.

For the three noise level tests shown in this section, the temperature span was 10 eV<T<100 eV, and the electron number density span was $1 \times 10^{22}\ m^{-3} < n_e < 10 \times 10^{22}\ m^{-3}$. The noise level was defined to be the ratio of the standard deviation of the noise to the peak amplitude of the signal. Noise levels of 0%, 1%, and 5% are shown below in Figures 4.1 – 4.3. There are two main results of these tests. The first is that is very difficult to resolve small temperatures with large number densities and vice versa. The second is that beyond noise levels of around 1% the system is no longer able to make accurate determinations across most of the parameter space. This is supported by experiences with real data, where the error in the fitted number density becomes very large compared to the nominal value if the noise percentage moves much beyond 1%. Some examples of temperature and number density fits with the peak emission levels and the noise percentages are also shown.

4.2.1 Noise level in real data

The 1% noise level limit predicted by the synthetic data analysis was supported by the real data fits. Shown below in Figure 4.4 are the results of fits for a shot in which the noise level is initially close to 1% and then grows reaching almost 4%. As the noise level grows, the fitter loses its ability to accurately find temperature and electron density. When presented with noisy data, the fit responds by pushing the temperature to zero and drives the uncertainty in the number density to be very large.

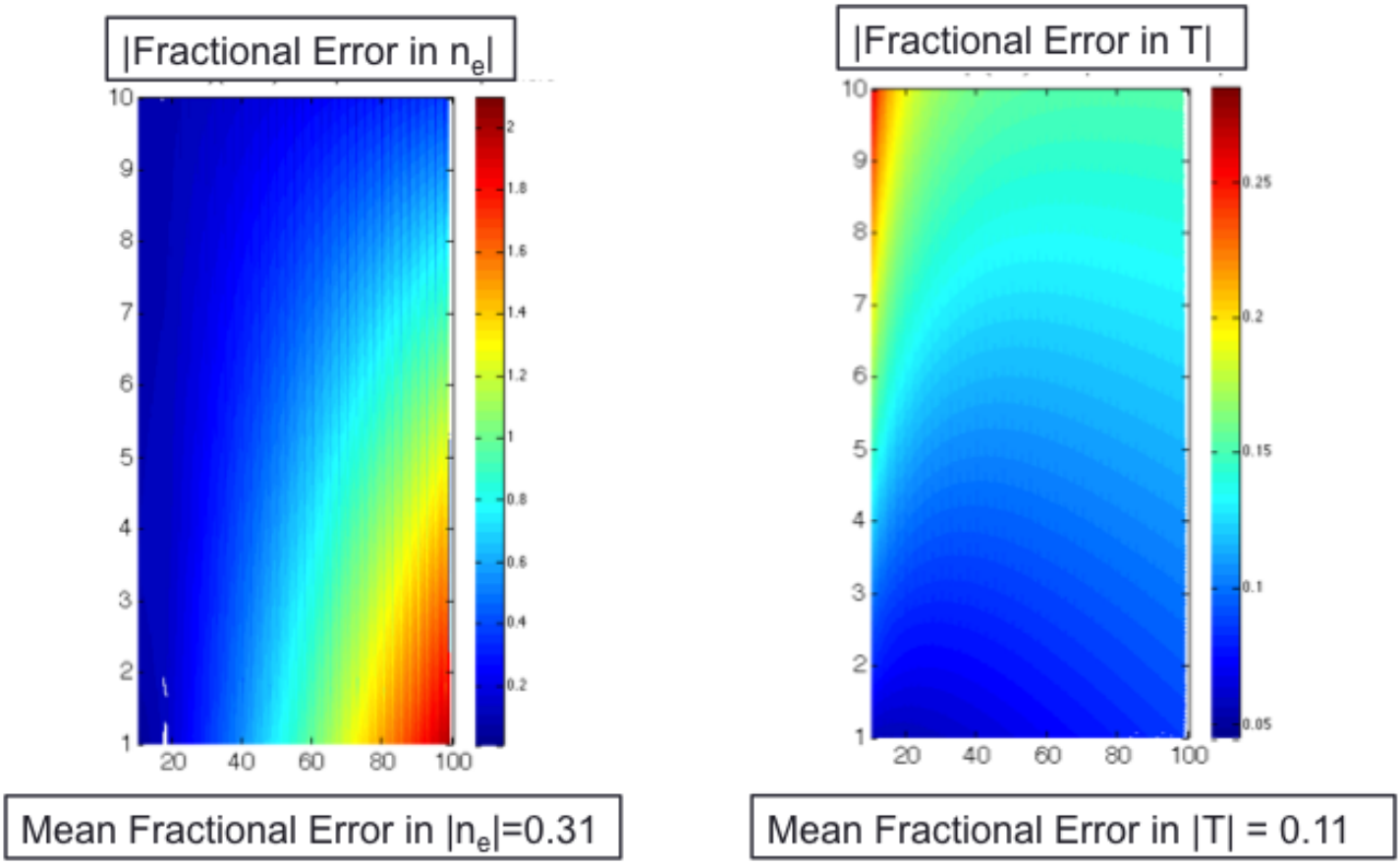

Figure 4.1 Left: The absolute value of the fractional error in electron number density; the fractional error across this region is 0.31 in number density. Right: The absolute value of the fractional error in temperature; the average fractional error is 0.11 in temperature. In both plots red indicates larger errors, although the scales differ between the two plots. The parameter space is $[10\text{ eV} < T < 100\text{ eV}] \times \left[1 \times 10^{22}\text{ m}^{-3} < n_e < 10 \times 10^{22}\text{ m}^{-3}\right]$. It is noteworthy that the error in number density (temperature) is largest when number density (temperature) is small while temperature (number density) is large.

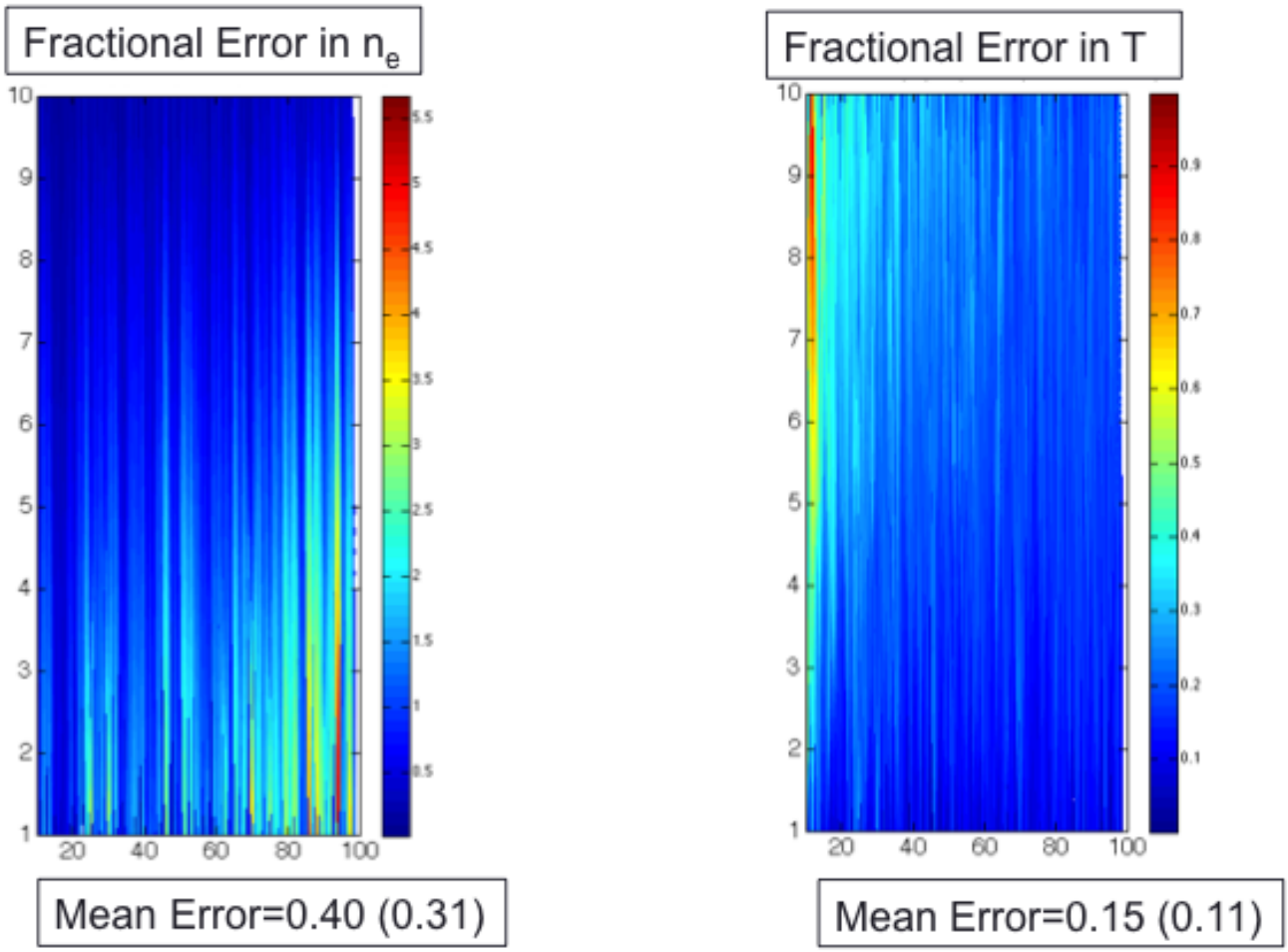

Figure 4.2 Introducing a 1% noise level, defined as the standard deviation of the noise divided by the signal's peak amplitude, into the synthetic data leaves the fractional error structure largely unchanged. Furthermore, the mean errors across the parameter space,$[10\text{ eV} < T < 100\text{ eV}] \times \left[1 \times 10^{22}\text{ m}^{-3} < n_e < 10 \times 10^{22}\text{ m}^{-3}\right]$, only increase by about 30% from 0.31 to 0.40 for number density and 0.11 to 0.15 for temperature. This 1% noise level is the threshold for succesful Fourier fitting.

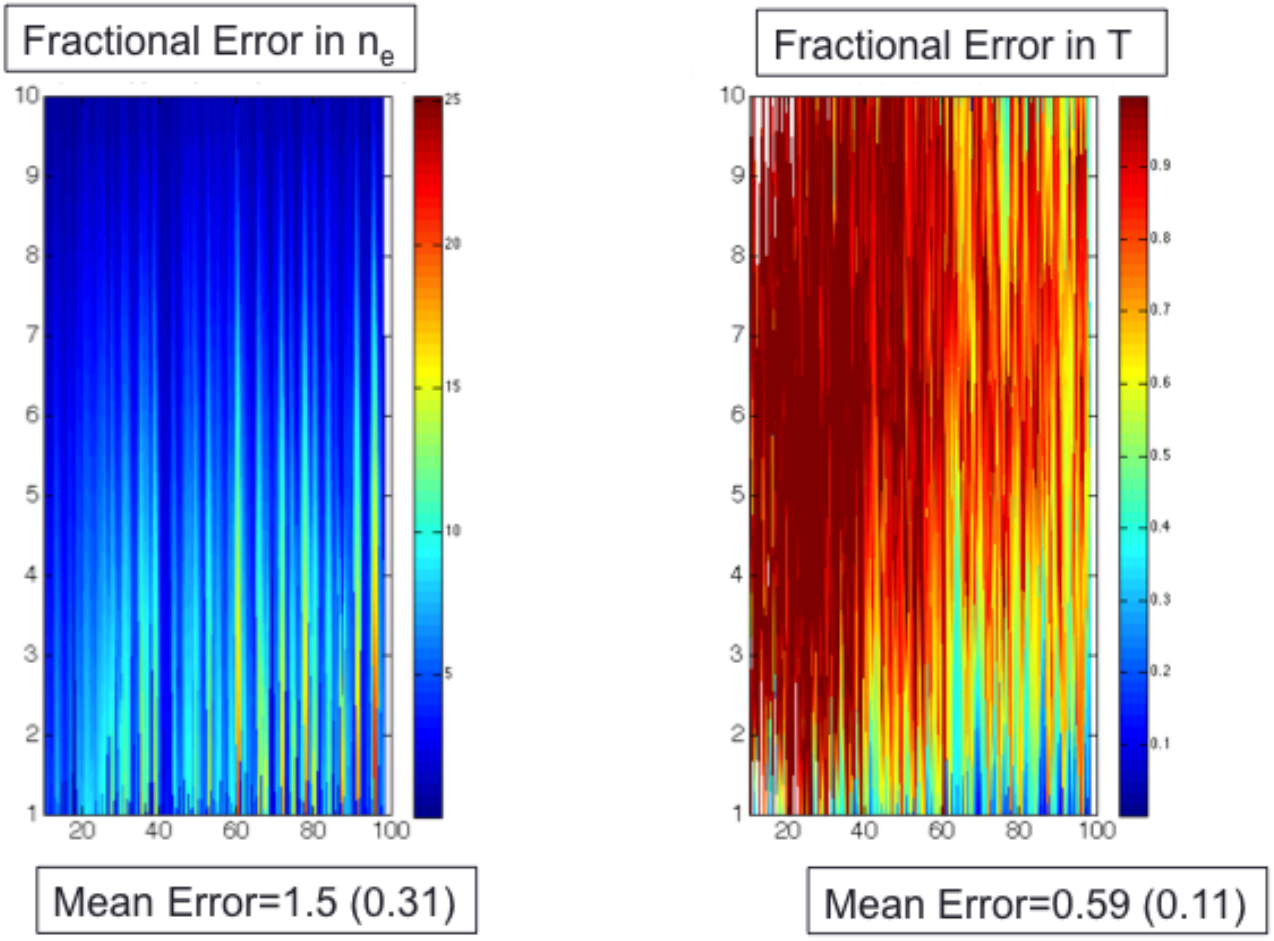

Figure 4.3 Introducing a 5% noise level dramatically degrades the performance of the Fourier fitter, as demonstrated by the increase in mean error in number density from 0.31 in the no-noise case to 1.5 with 5% noise added. Temperature also suffers increasing in mean error from 0.11 to 0.59. The parameter space, $[10\text{ eV} < T < 100\text{ eV}] \times \left[1 \times 10^{22}\text{ m}^{-3} < n_e < 10 \times 10^{22}\text{ m}^{-3}\right]$, remained the same.

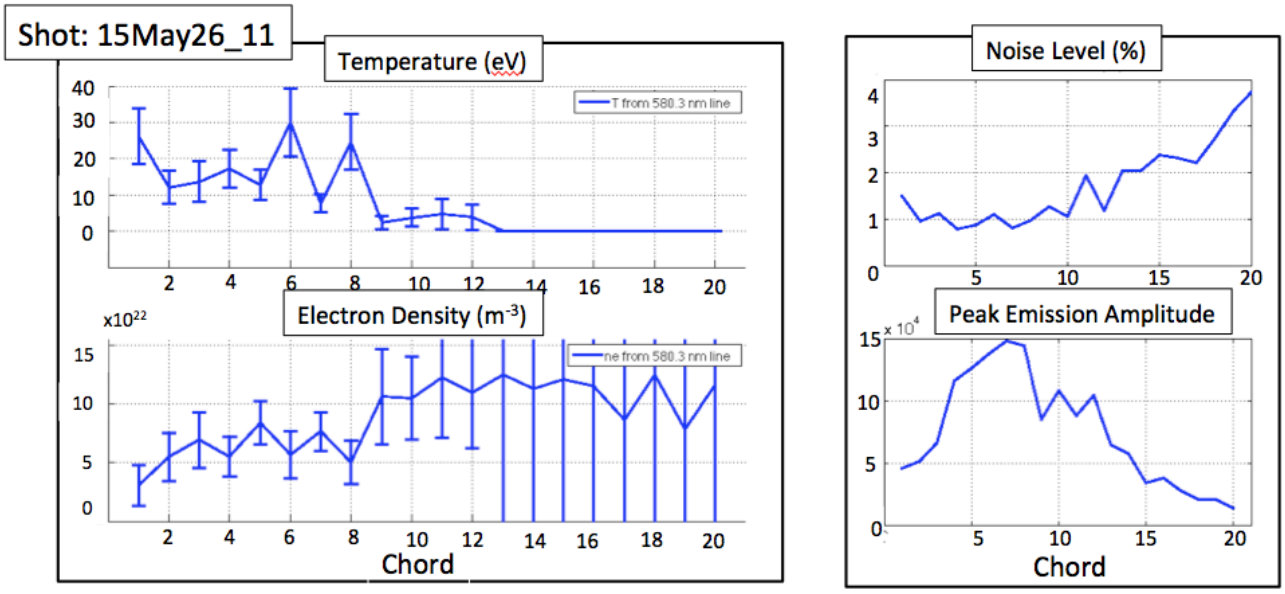

Figure 4.4 The noise level [top right], defined as the ratio of the standard deviation of the signal in a dark region to the peak signal amplitude, is plotted as a function of chord. Around chord 10 the noise level starts to increase above the 1% noise limit. This rise in noise level corresponds to growing error in electron density [bottom left], minimal temperature [top left], although not necessarily reduced signal strength [bottom right].

4.3 Real data fit

The 1% noise level is restrictive for the data currently being produced from the ZaP-HD plasma. A sample result in which the noise level was sufficiently small across all chords is shown below in Figure 4.5 – 4.10. Qualitatively, the results demonstrate the expected interdependencies between temperature and emission, i.e. when temperature is measured as low, the emission level of the CIV line is also measured as low. Quantitatively, the values for electron density through the apparent center of the plasma and magnetic field at the apparent edge match with the values measured by the interferometer and the magnetic field probes, respectively. The data can be seen in Figure 4.5. Sample fits of the chords can be seen in Figure 4.6 and Figure 4.7. The measured parameters for each chord are shown in Figure 4.8–4.10. The results agree with the other diagnostics on the ZaP-HD machine.

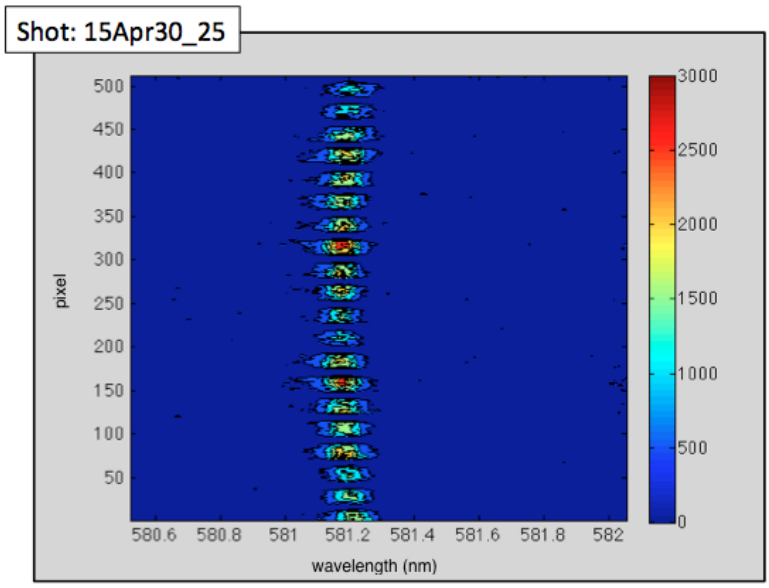

Figure 4.5 A contour plot of the intensities captured on the spectrometer. Wavelength in nm is shown on the horizontal axis, while pixel number is shown on the vertical axis.

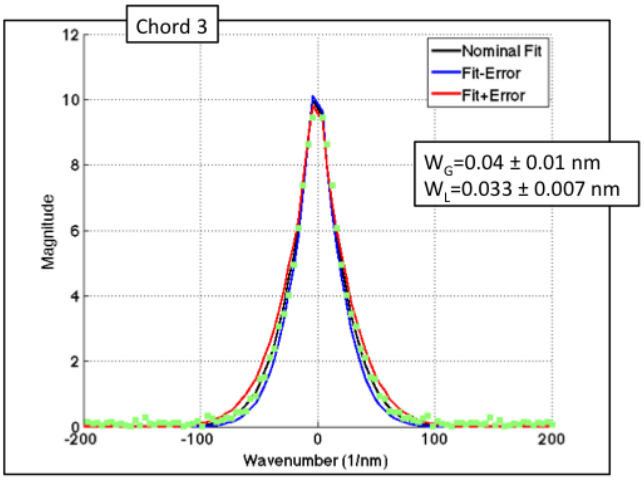

Figure 4.6 The results of the FFT LSQ fitter applied to the third chord of the spectrometer. The data are shown in green. The black line is the nominal fit. The blue and red lines represent the 95% confidence interval. A FWHM of 0.04 nm in the Gaussian component corresponds to a temperature of 10 eV. A FWHM of 0.033 nm in the Lorentzian component corresponds to a density of $5.9 \times 10^{22} \mathrm{m}^{-3}$. Note that the sharp peak is a result of the discrete spacing and not the fit function.

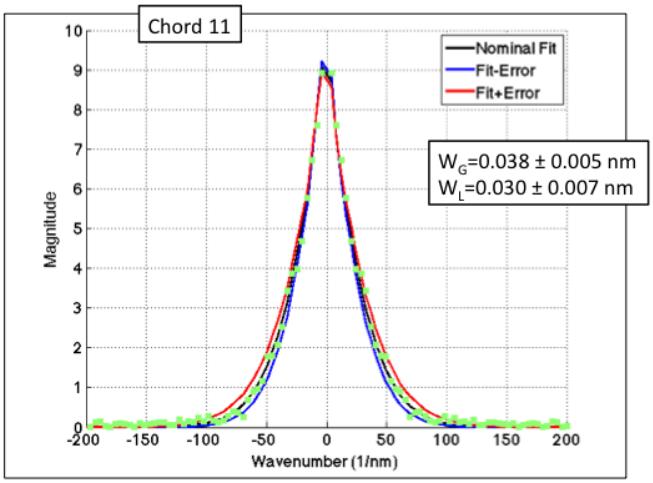

Figure 4.7 The results of the FFT LSQ fitter applied to the eleventh chord of the spectrometer. The data are shown in green. The black line is the nominal fit. The blue and red lines represent the 95% confidence interval. A FWHM of 0.038 nm in the Gaussian component corresponds to a temperature of 8.7 eV. A FWHM of 0.030 nm in the Lorentzian component corresponds to a density of $5.4 \times 10^{22} \mathrm{m}^{-3}$. Note that the sharp peak is a result of the discrete spacing and not the fit function.

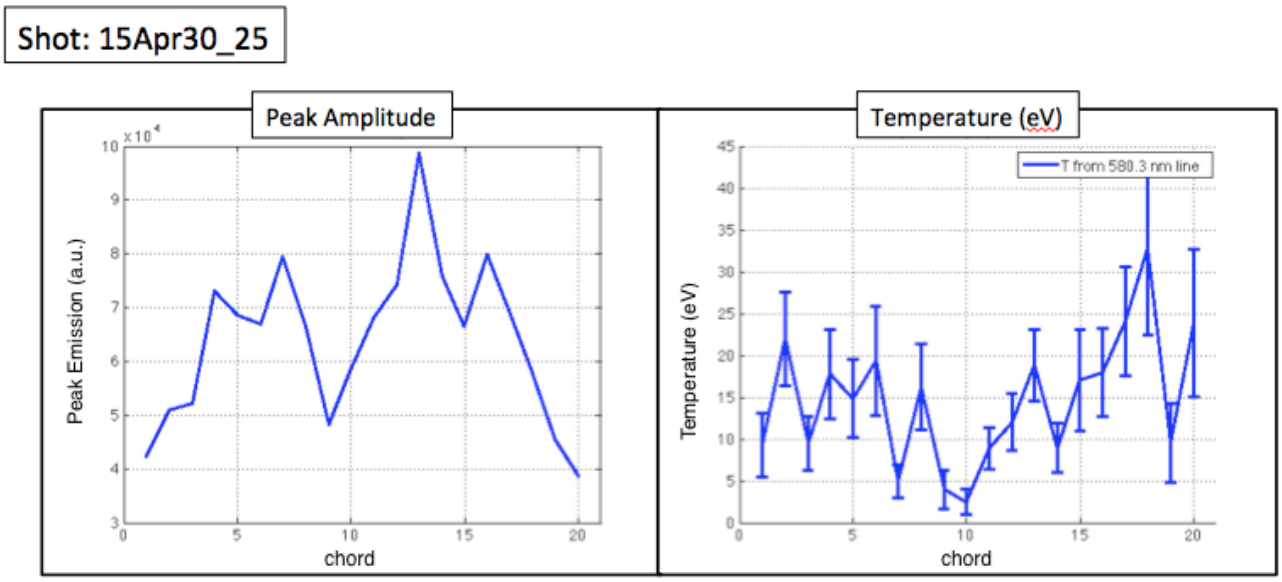

Figure 4.8 The peak emission amplitude and temperature for each chord.

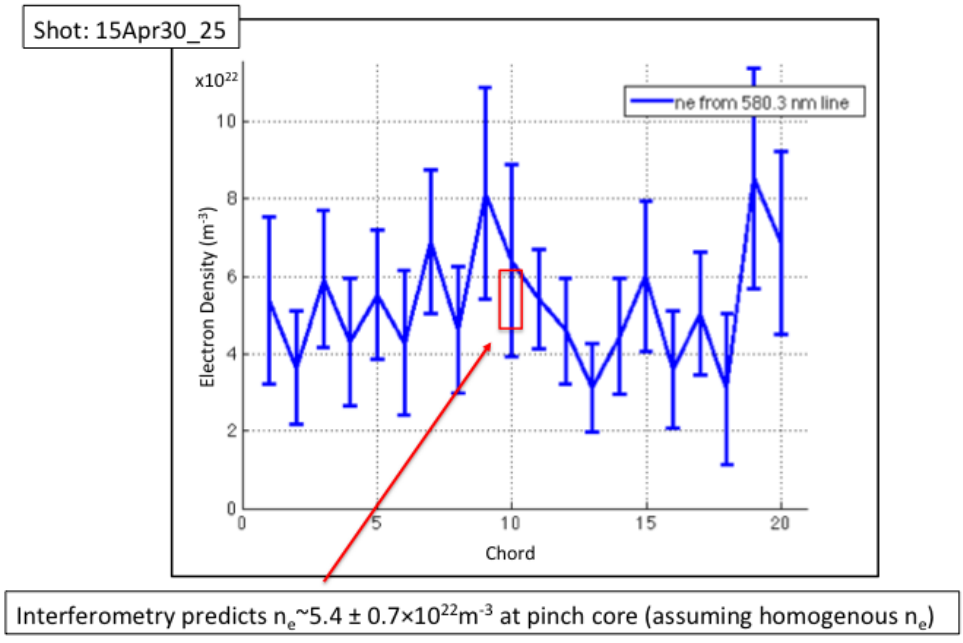

Figure 4.9 The electron density measured by the FFT LSQ fitter. The density measured by the interferometer, assuming an homogenous pinch, agrees with the spectroscopic measurement.

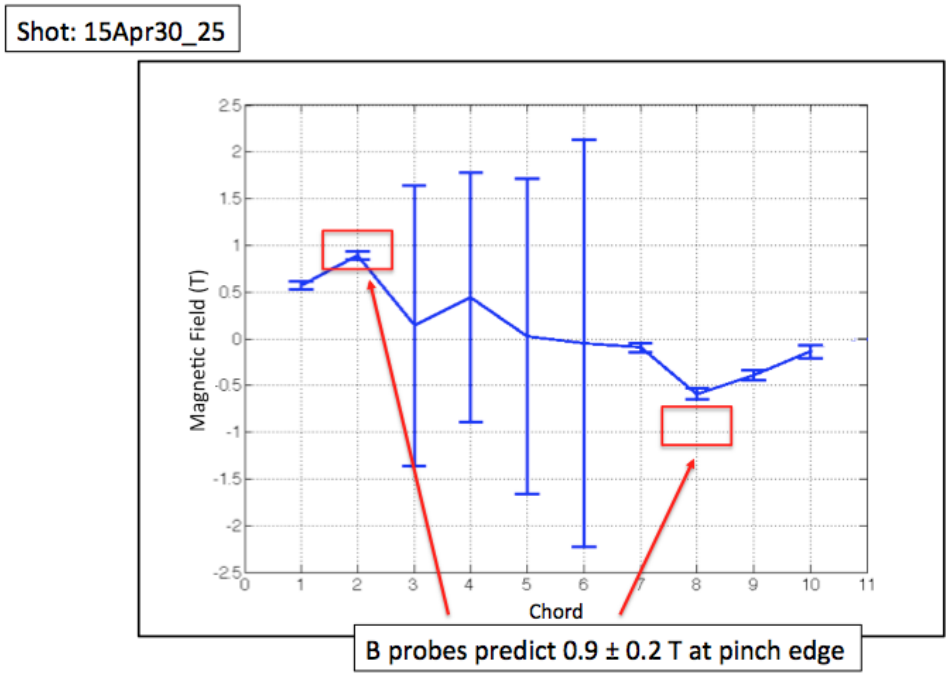

Figure 4.10 The magnetic field measured by the FFT LSQ fitter. The magnetic field measured by the magnetic probes on the inner wall, assuming that no plasma exists outside of the peak magnetic fields, agrees with the spectroscopic measurement.

Chapter 5

Conclusion and Future Work

This thesis has discussed the application of Fourier transform fitting to simultaneously resolve temperature, electron density, and magnetic field on the ZaP-HD experiment. The FFT LSQ fitter was found to perform accurately when the noise level, defined as the ratio of the standard deviation of the noise (found in a known dark region of the spectrum) to the peak signal amplitude, was around 1% or smaller. The results, when this criterion was achieved, were positive and strongly agreed with other diagnostics. The spectroscopic measurements of electron density at the center of the pinch overlapped with the chord-integrated measurement of the interferometer. Likewise, the spectroscopic measurement of the magnetic field on one edge of the plasma agreed with the edge field predicted by the magnetic probes. The limited spatial resolution of the spectroscopy system could explain the lack of agreement on the other side.

Although the reliability of the FFT LSQ code has been greatly improved, there still remain several important additions. The first is to provide true radial deconvolution. The Zeeman effect coupled with the polarimetry set up provide significant attenuation, $\propto \sin^2$, to inter-chordal contamination along the lines of sight of the spectrometer. However, true radial deconvolution requires that the outer shells of the concentric cylinders be subtracted from inner shells to ascertain electron density, temperature, and magnetic field as a function of radius. Removing contaminating shells

could also lead to improved fits, as gradients in temperature and electron density would cause the sum of chordal profiles to be different from the fit function (the pure Voigt profile). The second improvement to the FFT LSQ fitter could be to better characterize the instrument function to include an analytical description of its aberration. For this purpose a point source of known wavelength could be imaged through the spectrometer such that any wavefront aberrations would be entirely due to the spectrometer. The resulting image could then be decomposed in Zernike polynomials, an orthonormal basis set convenient for describing wavefronts in optical systems [18], to determine its analytical form; a similar scheme could be used on the telescope to see its effect on image quality. Lastly, the data analysis software could benefit from a graphical user interface (GUI) to eliminate usability challenges.

Appendix A

Matlab Code

What follows is the core Matlab code used to fit the captured profiles of the 581.2 nm CIV line. The code reads in the full data array output from WinSpec as an ASCII file, where there are 512×512 rows and 3 columns for each row corresponding to wavelength (horizontal pixel) location, vertical pixel location, and intensity. An instrument function is also required. The instrument function is stored in a tab-delimited ASCII file of 20 columns and 61 rows corresponding to the intensity of the instrument function for each of the 20 chords of the spectrometer with the pixel spacing set by the grating. Most of the computations are done in this main code. However, there are subfunctions that perform some plotting routines (not necessary) and smaller tasks like binning or calculation of the non-Fourier space Voigt profile. These functions are mentioned in the code below and were described by G. Vogman in the documentation of her code. The fitted temperatures and electron densities are returned in a plot and can be directly accessed through the variables, "output_data_fft" and "output_data_reg", for the Fourier and non-Fourier fits, respectively.

```
   breaklines
%%%%%%%%%%%%%%%%%%%%%%%%%%%%%%%%%%%%%%%%%%%%%%%%%%%%%%%%%%%%%%%%%%%%%%%%%%%%
%USER IMPORTANT STUFF:
%The data you want to fit is entered on line 155; it can either be a single
%file or multiple files (the code is set up to loop). The instrument
```

```
%function is specified on line 197. The default is for Zeeman
%splitting measurements. Everything else should work as is. You will need
%to get the directory path right for both of these.


%This code is a modification to the code developed by G. V. Vogman (and
%documented in G. V. Vogman and U. Shumlak, 2011). This code analyzes the
%581.2nm line of CIV. A least-squares fit of a Voigt profile is applied in
%the Fourier domain to determine the line broadening contributions due to
%temperature and electron density. The Fourier fit includes an instrument
%function (also Fourier transformed) in its fit function.
%A least-squares fit in the non-Fourier domain is used to determine the
%centroid of the profile for magnetic field calculations. For each fit the
%number of pixels is locked to 128. The bounds on the fit constrain the
%search to 1eV<T<800eV and 0.1x10^22 m^-3<ne<100x10^22 m^-3. The Fourier
%fit uses the magnitude of the Fourier spectrum rather than the real
%part, as used in Vogman, 2011. The Fourier fit does not employ any
%smoothing, also in contrast to Vogman, 2011. To reduce the length of this
%code, in order to make it more accessible, the synthetic data generator
%has been removed, as have some of her plotting routines.


%The following comments appeared in the original code:


% This code applies a basic fit and a Fourier fit to either (a) synthetic
% data or (b) actual data.  The words synthetic and simulated are used
% interchangeably.  For simulated data set simstring to 'simON', for actual
% data set simstring to 'simOFF'. For the case of actual data, this code
% will generate fits and plots of fits for each specified chord of data.
% The chord(s) is/are specified in the outer for-loop.  This code was used
% to generate Fig 1, Fig 2, and Fig 4 in the paper G. V. Vogman and U.
% Shumlak, "Deconvolution of Stark broadened spectra for multi-point
```

```
38 % density measurements in a flow Z-pinch," Review of Scientific Instruments
39 % 82 (10), 0034-6748 (2011).
40 %
41 % This file performs a least-squares fit to ICCD data in order to determine
42 % the temperature and density associated with a given spectral line.  The
43 % user must manually define which data to use (e.g. the wavelength range).
44 % Once a given range is defined,the ICCD data is assumed to have a Voigt
45 % profile, which is defined as the convolution of a Gaussian function with
46 % a Lorentzian function.  The Gaussian full width half max (FWHM) is
47 % related to the ion temperature and the Lorentzian FWHM is related to the
48 % electron density.  The ICCD data can either be real or simulated as
49 % specified by the user. A least squares fit is performed in two ways,
50 % first using a direct means to fit the convolution (this is called a
51 % "basic," or "regular" fit) and second by Fourier
52 % transforming the data and performing the fit in the Fourier domain.
53 % Data can be either simulated ('simON') or actual ICCD data ('simOFF').
54 %
55 % PREDEFINED CONSTANTS:
56 %           W = e- impact param see S. S. Harilal, C.V. Bhindhu paper 1997
57 %           c = speed of light in m/s
58 %   ioncenter = the center wavelength of ion line of interest
59 %          KB = Joules/eV
60 %           m = ion mass
61 %   simstring = 'simOFF' for actual data, 'simON' for simulated data
62 %
63 % FUNCTIONS USED
64 %   fitVoigtConvolveLG
65 %       Inputs: W, m, c, xsp, N, T, ioncenter, ioncenter
66 %       Output: Voigt profile
67 %       Description: Given density N and temperature T, construct a Voigt
68 %       profile centered at ioncenter using spacing defined by xsp.
69 %   fitVoigtfittingfunc
70 %       Inputs: m,c,W,x,vdata,ioncenter,weights,P
```

```
71 %               P is vector of unknown parameters that is to be optimized
72 %               weights is a string that is generally set to 'off'
73 %       Outputs: a residual defined by (convolution(L,G)-data).^2
74 %       Description: when performing a least squares fit of a convolution
75 %       with unknown parameters P (which are to be determined)
76 %       to the data, fitVoigtfittingfunction defines the residuals that are
77 %       to be minimized by the Matlab function fminsearch.  So the function
78 %       outputs a value that fminsearch attempts to minimize by varying hte
79 %       parameters P.
80 %   findGLWidths
81 %       Inputs: W, m, c, xsp, N, T, ioncenter
82 %       Output: [GaussianWidth, LorentzianWidth]
83 %       Description: Given temperature and density, determines associated
84 %       Gaussian and Lorentzian full width at half max.
85 %   genFakeError
86 %       Input: simx, simVdata
87 %       Output: [fakeError,mystrarray]
88 %       Description: takse (x,y) simulated Voigt profile data and generates
89 %       a vector of "fake error" - i.e. of noise that can include a
90 %       contaminating line.  This fake error" can be generated using the
91 %       (x,y) data or not using it.
92
93
94 close all;
95 clear all;
96
97 %add the path for access to Genia's functions
98 addpath('StarkFits2011')
99
100 % Instrument temperatures. These are only used for the non-Fourier fit and
101 % thus they should be left alone (not physically meaningful as the
102 % instrument function is not particularly Gaussian--actually appears to be
103 % more Lorentzian).
```

```
104 load instTemp80313019.dat
105 instTemp=instTemp80313019;
106
107
108
109 % Physical constants.
110 W=2.8e-2;         % e- impact parameter angstroms
111 %(I was not able to find this quantity in the paper
112 %S. S. HARILAL, C. V. BINDHU Genia cites.
113 c=3e8;            % speed of light in m/s
114 KB=1.6e-19;        %Boltzmann's constant in J/eV
115 m=12*1.67e-27;     % ion mass
116 % centroid wavelength in nm
117 %If you want to fit to the brighter line at 580.3, set 580.3 as ioncenter
118 %and set ioncenter2 to be 581.2.
119 ioncenter=581.2;
120 ioncenter2=ioncenter;
121
122
123
124 % Toggles.
125 % NOTE:
126 % In general weights should be 'off.'  However, if there is a compelling
127 % reason to do a regular fit with weights, this can be used as a switch to
128 % turn weights off and on.
129 weights='off';                              % generally weights are off
130 co=['b';'r'];                               % define colors for plotting
131 saveplotsString='off';                      % save plots? 'on' or 'off'
132 n=128;
133
134
135
136
```

```
137
138 %%%%%%%%%%%%%%%%%%%%%%%%%%%%%%%%%%%%%%%%%%%%%%%%%%%%%%%%%%%%%%%%%%%%%%%%
139 %the code begins in earnest here:
140
141
142 %Each run through the loop produces a
143 % "basic" fit and a "Fourier" fit.
144 % In the case of actual data, if all the chords are to be analyzed, the
145 % for-loop should read:
146 %       for mych = 1:20
147 % If only one chord is to be analyzed (for example chord 3) then the
148 % for-loop should read
149 %       for mych = 3
150
151
152 %Choose the files to be analyzed; this can be multiple files specified
153 %using Matlab's character matching, e.g. files=dir('.../15apr30*.txt')
154 %would analyze all the files from the directory .../ that start with
155 %15apr30 and end with .txt.
156 files=dir('/Users/lmcgonigle/Desktop/Code/15apr3025_1.txt');
157
158
159 for f=1:length(files)
160
161     fname=files(f).name
162     data_in_raw=dlmread(fname,',');
163
164     %take raw data, format it for contour plotting, and bin it.
165     %dat{1}=wavelength, dat{2}=y pixel, and dat{3}=intensities.
166     %binned{i} holds wavelength and intensity for each chord.
167     [ dat,chord_indexes, binned] = data_formatter( data_in_raw );
168     data_in(:,1)=binned{1}(1,:);
169
```

```
170     %reformatting binned data for Genia's code
171     for i=2:21
172         data_in(:,i)=binned{i-1}(2,:);
173     end
174
175
176     wave=data_in(:,1);              %pick out wavelength column
177     intensity=data_in(:,2:21);      %pick out intensity data for all chords
178
179     % Background subtraction across whole chord
180     for ch=1:20
181         backgr=min(abs(intensity(:,ch)));
182         intensity(:,ch)=intensity(:,ch)-backgr;
183     end
184
185     %turn on contourplot to see what the raw data looks like;
186     %the plots are windowed around the 581.2nm line.
187
188     contourplot=0;
189     if contourplot==1
190         figure
191         contour(dat{1}(:,217:344), dat{2}(:,217:344), dat{3}(:,217:344))
192         colorbar;
193     end
194
195
196     %Read in the instrument function
197     inst=dlmread('inst_func_4_0_1.txt');
198     %the instrument function is over 61 pixels and needs to be matched to
199     %the length of the Voigt profile for deconvolution--zero-pad!
200     new_inst=zeros(n,20);
201     inst_center=31;
202
```

```
203
204
205     %Initialize a loop for looking at multiple peaks.
206     for peaknumber=1:1
207
208         %Loop over each chord of a peak
209         for mych=1:20
210
211             %center the instrument function w/r to the data
212             new_inst(n/2:n/2+length(inst(:,mych))-inst_center,mych)=...
213                 inst(inst_center:end,mych);
214             new_inst(n/2-inst_center+1:n/2,mych)=inst(1:inst_center,mych);
215
216             % Select range of data that is of interest
217             indexes=200:(length(wave)-200);
218
219             %find the pixel location (center) of the desired peak
220             if peaknumber==2
221                 [ign, center]=max(intensity(:,mych));
222             else
223                 [ign secpeakind]=min(abs(wave-ioncenter2));
224                 [ign, center]=max(...
225                     intensity(secpeakind-50:secpeakind+50,mych));
226                 center=center+secpeakind-50-1;
227             end
228
229             %set the pixels of interest for fitting
230             indexes=center-n/2:center+n/2;
231             %pick out the wavelengths
232             xdata=wave(indexes)';
233             %maker a denser set of wavelengthts for regular fit
234             xx=linspace(min(xdata),max(xdata),1000);
235             xsp=linspace(min(xdata),max(xdata),129);
```

```
236             %pick out the intensity
237             lineIntensity=intensity(indexes,:);
238             %line intensity for chord mych
239             V=lineIntensity(:,mych)';
240             %perform background subtraction for intensity sample:
241             V=V-min(V);
242             noise_perc(mych)=std(intensity(450:500,mych))/max(V);
243             %normalize the line intensity (makes the amp fit param easier)
244             vdata=V/max(V);
245
246
247
248
249             % Regular LSQ fit to find ne, T, centroid, and amplitude
250             options=optimset('MaxFunEvals',1e6, 'MaxIter',...
251                 1e7,'Display','off');
252             result=fminsearch(@(P) fitVoigtfittingfunc(m,c,W,xdata,...
253                 vdata,ioncenter,weights,P),[7e16 80 ioncenter 10],options);
254             regN=result(1);
255             regT=result(2);
256             regC=result(3);
257             regA=result(4);
258
259             % Using optimized parameters from regular fit, construct Voigt
260             % profile and compute the FWHM of the associated Gaussian and
261             % Lorentzian
262             voigtRegularFit=regA*fitVoigtConvolveLG(W,m,c,xx,regN,...
263                 regT,ioncenter,regC);
264             [regGW,regLW]=findGLWidths(W,m,c,xx,regN,regT,ioncenter);
265
266
267             % Then to use the nlinfit function in Matlab to compute the
268             % covariance and residuals to determine confidence
```

```
269             % intervals in addition to the optimized parameters
270             A=regC;
271             %cent=regC;
272             % Nonlinear regression for purposes of computing error
273             % calculation.
274             options=statset('Robust','on','MaxIter',1e7,...
275                 'TolFun',1e-10,'Display','off');
276
277
278             [regParam,regResidual,regJacob,regCov,regMSE] =...
279                 nlinfit(xdata,vdata,@(param,X) ...
280                 regfitnonlin(m,c,W,A,ioncenter,param,X),...
281                 [regLW regGW regC regA]);
282             regnonlinGW=regParam(2);
283             regnonlinLW=regParam(1);
284
285             % Compute 95% confidence interval
286             regConfidenceInterval2=nlparci(regParam,regResidual,...
287                 'covar',regCov);
288             regConfidenceInterval=nlparci(regParam,regResidual,...
289                 'jacob',regJacob);
290
291             % Compute error in FWHM
292             regDeltaW=0.5*(regConfidenceInterval(:,2)...
293                 -regConfidenceInterval(:,1));
294             % Compute error in Lorentzian FWHM
295             regErrorWL=regDeltaW(1);
296             % Compute error in Gaussian FWHM
297             regErrorWG=regDeltaW(2);
298             cent_err(mych)=regDeltaW(3);
299             % Compute 95% confidence density range
300             regnonlinN=10*regnonlinLW/(W*2e-16);
301             regDeltaN=(regErrorWL)/(W*2e-16);
```

```
302
303             % Compute 95% confidence temperature range
304             regnonlinT=(regnonlinGW/ioncenter)^2*m*c^2/(KB*8*log(2));
305             regDeltaT=((regErrorWG)/ioncenter)^2*m*c^2/(KB*8*log(2));
306
307
308
309
310
311
312 %Here begins the Fourier fitting
313
314             % Fourier transform of data (n=128)
315             fftx=xdata(1:n);
316             vdatas=vdata(1:n)';
317             L=fftx(end)-fftx(1);
318             plotxspace=0;
319             if plotxspace==1
320                 figure
321                 plot(fftx, vdatas)
322             end
323             % Define the wave number using
324             k=(2*pi/L)*[0:n/2-1 -n/2:-1];
325
326             %these shifts center the fft spectrum around 0.
327             fftvdata=fft(fftshift(vdatas));
328             fftdata=fftshift(fftvdata);
329             kn=fftshift(k)';
330
331             %For fitting we want the magnitude of the Fourier spectrum.
332             fftdatanormal=abs(fftdata);
333             smfftdatanormal=abs(fftdata);
334
```

```
335             % The center (DC offset) is not included in the fit array
336             indexCenter=find(fftdatanormal~= max(fftdatanormal));
337             kcenter=kn(indexCenter);
338             fftdatanormal2=smfftdatanormal;
339             fftdatacenter=fftdatanormal2(indexCenter);
340
341             %Find the FFT of the instrument function of this chord
342             fft_inst=fft(new_inst(:,mych));
343             fft_inst_center=fftshift(abs(fft_inst(indexCenter)));
344
345
346
347
348             %Define the fit function,FFT(data)=FFT(G)*FFT(L)*FFT(Inst)
349             fwidths=@(B,kk) B(1)*exp(-B(2)^2.*kcenter(kk).^2/(16*log(2))...
350                 -B(3).*abs(kcenter(kk))/2).*fft_inst_center(kk);
351
352
353             % Apply a least squares fit to Fourier transformed data.
354             % B(1)=amplitude,B(2)=Gaussian FWHM, and B(3)=Lorentzian FWHM
355             options=optimset('MaxFunEvals',1e8, 'MaxIter',1e10,...
356                 'Diagnostics','off','Display','off');
357             [widthsLSQ, resnorm, residual]=lsqcurvefit(fwidths,...
358                 [1,0.5, 0.01 ],1:length(kcenter),fftdatacenter,...
359                 [1 5.0e-3 5.6e-4],[100 0.14 0.56],options);
360             % The limits, [1 5.0e-3 5.6e-4],[100 0.14 0.56], require the
361             % temperature to be between 1 eV and 800 eV and ne to be within
362             % 0.1x10^22 m^-3 and 100x10^22 m^-3.
363
364
365
366             % To determine the residuals and covariance to determine the
367             % 95% confidence interval; the optimized parameters from above
```

```
368             % are used as the initial estimates.
369             options=statset('Robust','on','Display','off');
370             [fftParam,fftResidual,fftJacob,fftCov,fftMSE] = nlinfit(...
371                 1:length(kcenter),fftdatacenter,fwidths,...
372                 [widthsLSQ(1) widthsLSQ(2) widthsLSQ(3)]);
373             fftConfidenceInterval=nlparci(...
374                 fftParam,fftResidual,'covar',fftCov);
375
376             % Determine the 95% confidence range
377             fftErrorW=0.5*(fftConfidenceInterval(:,2)...
378                 -fftConfidenceInterval(:,1));
379             fftErrorWL=fftErrorW(2);
380             fftErrorWG=fftErrorW(3);
381
382             % Determine the 95% confidence range for the density
383             fftnonlinN=10*fftParam(3)/(W*2e-16);
384             fftnonlinNhigh=10*(fftParam(3)+fftErrorWL)/(W*2e-16);
385             fftnonlinNlow=10*(fftParam(3)-fftErrorWL)/(W*2e-16);
386             fftDeltaN=(fftnonlinNhigh-fftnonlinNlow)/2;
387
388             % Determine the 95% confidence range for the temperature
389             fftnonlinT=(fftParam(2)/ioncenter)^2*m*c^2/(KB*8*log(2));
390             fftnonlinThigh=((fftParam(2)+fftErrorWG)/ioncenter)^2 ...
391                 *m*c^2/(KB*8*log(2));
392             fftnonlinTlow=((fftParam(2)-fftErrorWG)/ioncenter)^2 ...
393                 *m*c^2/(KB*8*log(2));
394             fftDeltaT=(fftnonlinThigh-fftnonlinTlow)/2;
395
396
397             %plot the Fourier fit (if on)
398             fourierplot=1;
399             if fourierplot==1
400                 figure
```

```
401                 grid on
402                 set(gcf,'color','w');
403                 set(gca,'fontsize',18);
404                 hold all
405                 plot(kcenter,fwidths(widthsLSQ,1:length(kcenter)),...
406                     'linewidth',1.2,'color','k')
407                 plot(kcenter,fwidths(widthsLSQ+transpose(fftErrorW),...
408                     1:length(kcenter)),'linewidth',1.2,'color','b')
409                 plot(kcenter,fwidths(widthsLSQ-transpose(fftErrorW),...
410                     1:length(kcenter)),'linewidth',1.2,'color','r')
411                 scatter(kcenter,fftdatacenter,50,...
412                     zeros(1,length(kcenter))+1,'s','filled')
413                 xlabel('Wavenumber (1/nm)')
414                 xlim([-200 200])
415                 ylabel('Magnitude')
416                 legend('Nominal Fit', 'Fit-Error', 'Fit+Error')
417                 hold off
418             end
419
420
421
422
423
424
425             % Pull out parameters from variable widthsLSQ and paramsLSQ
426             %and check that nlinfit and lsqcurvefit are consistent.
427             widthsA=widthsLSQ(1);
428             widthsGw=widthsLSQ(2);
429             widthsLw=widthsLSQ(3);
430
431             widthsN=10*widthsLw/(W*2e-16);
432             widthsT=(widthsGw/ioncenter)^2*m*c^2/(KB*8*log(2));
433
```

```
434             widthsA_errh=widthsA+fftErrorW(1);
435             widthsA_errl=widthsA-fftErrorW(1);
436             widthsN_errh=10*(widthsLw+fftErrorWL)/(W*2e-16);
437
438
439             %if widths-uncertainties are negative, set to almost zero.
440             if widthsLw-fftErrorWL<0.001
441                 widthsN_errl=0.01;
442             else
443                 widthsN_errl=10*(widthsLw-fftErrorWL)/(W*2e-16);
444             end
445             widthsT_errh=((widthsGw+fftErrorWG)/ioncenter)^2 ...
446                 *m*c^2/(KB*8*log(2));
447             if widthsGw-fftErrorWG<0.001
448                 widthsT_errl=0.01;
449             else
450                 widthsT_errl=((widthsGw-fftErrorWG)/ioncenter)^2 ...
451                     *m*c^2/(KB*8*log(2));
452             end
453
454             widthsfftG=exp(-widthsGw^2*kn.^2/(16*log(2)));
455             widthsfftL=exp(-widthsLw*0.5*abs(kn));
456
457
458             % Determine what Fourier fit looks like in physical space.
459             % Take the inverse Fourier transform and interpolate onto a
460             % denser setof x data points. (L:)I'm not sure this still
461             % works b/c of including the instrument function in the fit...
462             widthsfftAnal=widthsA*widthsfftG.*widthsfftL;
463             physSpaceFit=fftshift(abs(ifft(widthsfftAnal)));
464             physSpaceFitxx=interp1(fftx,physSpaceFit,xx);
465
466             % Determine centroid for fft least squares fit (does not have
```

```
467             % centroid as one of its parameters). Do this only for real
468             % data. Then generate a Voigt profile vector that is the
469             % "least squares fit."  Optimization of the centroid usually
470             % gives unreasonable values.
471             centroid=fminsearch(@(b) sum(abs(fitVoigtConvolveLG(...
472                 W,m,c,xdata,widthsN,widthsT,ioncenter,b)/max(...
473                 fitVoigtConvolveLG(W,m,c,xdata,widthsN,...
474                 widthsT,ioncenter,b))-vdata)),ioncenter);
475
476                 physSpaceFit2=widthsA*fitVoigtConvolveLG(W,m,c,xx,...
477                     widthsN,widthsT,ioncenter,centroid);
478                 physSpaceFit2_err1=widthsA_errh*fitVoigtConvolveLG(...
479                     W,m,c,xx,widthsN_errh,widthsT_errh,ioncenter,centroid);
480                 physSpaceFit2_err2=widthsA_errl*fitVoigtConvolveLG(...
481                     W,m,c,xx,widthsN_errl,widthsT_errl,ioncenter,centroid);
482
483
484
485
486             %Store the data for both the Fourier and non-Fourier fits.
487             output_data_fft{peaknumber}(1,mych)=[fftnonlinT];
488             output_data_fft{peaknumber}(2,mych)=[fftDeltaT];
489             output_data_fft{peaknumber}(3,mych)=[fftnonlinN/10^16];
490             output_data_fft{peaknumber}(4,mych)=[fftDeltaN/10^16];
491             output_data_reg{peaknumber}(1,mych)=[regnonlinT];
492             output_data_reg{peaknumber}(2,mych)=[regDeltaT];
493             output_data_reg{peaknumber}(3,mych)=[regnonlinN/10^16];
494             output_data_reg{peaknumber}(4,mych)=[regDeltaN/10^16];
495             output_data_reg{peaknumber}(5,mych)=regC;
496             output_data_reg{peaknumber}(6,mych)=regDeltaW(3);
497
498
499
```

```
500
501         end
502     end
503
504
505     %Magnetic field calculations using the conversion mentioned in
506     %Golingo, 2010.
507     i2=1;
508     for i=1:2:19
509
510         output_data_reg{peaknumber}(7,i2)=(output_data_reg{peaknumber}...
511             (5,i)-output_data_reg{peaknumber}(5,i+1))*(0.6/0.0126);
512
513         output_data_reg{peaknumber}(8,i2)=(sqrt(...
514             output_data_reg{peaknumber}(6,i)^2 ...
515             +output_data_reg{peaknumber}(6,i+1)^2))*(0.6/0.0126);
516         i2=i2+1;
517     end
518 end
519
520
521
522
523 %final summary plots of the parameters over chord:
524 summary_plots( output_data_fft, output_data_reg, ...
525     peaknumber,fname,noise_perc,intensity )
```

Bibliography

[1] U. Shumlak et al., "Equilibrium, flow shear and stability measurements in the Z-pinch", *Nucl. Fusion*, **49**, (2009).

[2] U. Shumlak et al., "The Sheared-Flow Stabilized Z-pinch", *Transactions of Fusion Science and Technology*, Vol. 61, (2012).

[3] R. J. Oberto et al., "Calibration of the Thomson Scattering System on the ZaP Experiment", APS Division of Plasma Physics, (November, 2009), poster presentation.

[4] J. P. Freidberg, "Ideal magnetohydrodynamic theory of magnetic fusion systems", *Review of Modern Physics*, Vol. 54, No. 3, (1982).

[5] B. B. Kadomtsev, *Reviews of Plasma Physics*, Vol. 2, New York: Consultants Bureau, (1966), p. 153.

[6] U. Shumlak and C. W. Hartman, "Sheared flow stabilization of the m=1 kink mode in Z pinches", *Phys. Rev. Lett.*, Vol. 75, 3285-8, (1995).

[7] U. Shumlak et al., "The Sheared-Flow Stabilized Z-Pinch", *Transactions of Fusion Science and Technology*, Vol. 61, (2012).

[8] U. Shumlak et al., "High Energy Density Z-Pinch Plasmas using Flow Stabilization: ZaP-HD", SSAP Symposium, (February, 2014), conference presentation.

[9] P. G. Carolan et al., "Observation of Zeeman Splitting of Spectral Lines from the JET Plasma", *Plasma Physics and Controlled Fusion*, Vol. 27, 10, (1985).

[10] P. F. Bernath, *Spectra of Atoms and Molecules*, New York: Oxford University Press, (1995).

[11] R. H. Dicke, "The Effect of Collisions upon the Doppler Width of Spectral Lines", *Physical Review Letter*, Vol. 89, 2, (1953).

[12] H. R. Griem, *Spectral Line Broadening by Plasmas*, New York: Academic Press, (1974).

[13] H. R. Griem, *Principles of Plasma Spectroscopy*, New York: Cambridge University Press, (2005).

[14] D. Salzmann, *Atomic Physics in Hot Plasmas*, New York: Oxford University Press, (1998).

[15] G. V. Vogman and U. Shumlak, "Deconvolution of Stark broadened spectra for multi-point density measurements in a flow Z-pinch", *Review of Scientific Instrument*, Vol. 82, 103504, (2011).

[16] D. J. Den Hartog and R. P. Golingo, "Telecentric viewing system for light collection from a z-pinch plasma", *Review of Scientific Instruments*, Vol. 72, No. 4, (2001).

[17] R. P. Golingo et al., "Zeeman splitting measurements in a high-temperature plasma", *Review of Scientific Instruments*, Vol. 81, 126104, (2010).

[18] M. Born et al., *Principles of Optics: Electromagnetic Theory of Propagation, Interference and Diffraction of Light*, 7^{th} ed., New York: Cambridge University Press, (1999).